EVALUATION AND IMPROVEMENT OF ATMOSPHERIC INFRARED SOUNDER (AIRS) ICE CLOUD RETRIEVALS

A Thesis

by

VOLKAN HUSEYIN FIRAT

Submitted to the Office of Graduate and Professional Studies of
Texas A&M University
in partial fulfillment of the requirements for the degree of

MASTER OF SCIENCE

Chair of Committee,	Shaima L. Nasiri
Committee Members,	Gerald R. North
	Anthony M. Filippi
Head of Department,	Ping Yang

August 2015

Major Subject: Atmopsheric Sciences

ABSTRACT

Clouds are still one of the largest uncertainties of the current climate models. While satellites provide suitable global datasets for comparing with cloud properties derived from models, satellite retrievals are inferences of cloud properties, rather than direct measurements, and therefore have errors. Therefore, it is important to evaluate satellite cloud products and gain advanced understanding of the products to accurately interpret the observations.

This study investigates Aqua AIRS version 6 Level 2 cloud thermodynamic phase, ice cloud optical thickness, and ice cloud effective diameter, which released in April, 2013 and are available for all 13 years of the AIRS record. A filtering and gridding algorithm is used to create customized globally gridded datasets to evaluate the effects of satellite's viewing zenith angle, effective cloud fraction, cloud layers, cloud top temperature, time of the year, and geographic region.

Viewing zenith angle does not strongly affect AIRS ice-phase, but higher viewing zenith angles lead to more water and fewer unknown pixels; the viewing zenith angle dependence is not strongly affected by the time of the year. Higher effective cloud fraction yields more ice- and water-phase, and less unknown-phase retrievals. Also, higher effective cloud fractions lead to greater values of ice cloud optical thickness. In addition, especially in high latitudes, ice-phase frequency is greater for two-layer clouds than single-layer clouds. On the other hand, water- and unknown-phase frequencies are greater for single layer clouds. Also, higher viewing zenith angles slightly decrease upper cloud top temperature. Approximately 90% of ice-phase cases have upper cloud top temperature values between 210 K and 235 K, ∼80% of water-phase cases are found at 243-273 K upper cloud top temperature interval, and

∼80% of the unknown cases have upper cloud top temperature values between 230 and 264 K. For ice cloud optical thickness and ice cloud effective diameter, no strong effects of satellite viewing zenith angle or cloud layering are observed.

DEDICATION

This study is dedicated to my wife, Sema Firat, to my sister, Alev Gul Firat, to my parents, Altun Firat and Kazim Firat, and to my grandfather, Huseyin Firat.

ACKNOWLEDGEMENTS

I would like to thank Dr. Shaima L. Nasiri not only for guiding me wisely, but also for supporting and encouraging me as a family. I thank Dr. Brian H. Kahn for providing the data used and for his valuable suggestions. I would also like to thank my committee members, Dr. Gerald R. North and Dr Anthony M. Filippi, for their suggestions to improve this study.

This study is partially supported by the Republic of Turkey Ministry of National Education in the name of the Turkish State Meteorological Service.

TABLE OF CONTENTS

Page

ABSTRACT ii

DEDICATION iv

ACKNOWLEDGEMENTS v

TABLE OF CONTENTS vi

LIST OF FIGURES vii

LIST OF TABLES x

1. INTRODUCTION 1

2. DATA AND METHODS 9

2.1 The Atmospheric Infrared Sounder (AIRS) Version 6 Cloud Products 9
2.2 Uniform Space-Time Gridding Algorithm 13
2.2.1 STG algorithm application 14

3. RESULTS 19

3.1 Satellite's Viewing Zenith Angle Effect 20
3.2 Effective Cloud Fraction Effect 24
3.3 Cloud Layering Effect 30
3.4 Upper Layer Cloud Top Temperature Effect 36

4. CONCLUSIONS 41

REFERENCES 45

LIST OF FIGURES

FIGURE Page

1.1 Illustration of cloudy sky infrared radiative transfer equation terms. 5

2.1 Scan geometry of AIRS/AMSU at nadir view. Solid circles and dashed circle in the upper right corner indicate AIRS FOV and AMSU FOR, relatively. This figure is adapted from Aumann et al. (2003). 10

2.2 Schematic view of AIRS cloud thermodynamic phase. 11

2.3 Global distributions of filtered and gridded Aqua AIRS v6 L2 ECFLow (top), ECFMid (middle), and ECFHigh (bottom) for 2003 to 2012. The frequency is the number of observed ECFLow, ECFMid, or ECFHigh divided by the total number of observation with ECF retrieval. 18

3.1 Global distribution of filtered and gridded Aqua AIRS v6 L2 cloud fraction for 2003 to 2012. The frequency (cloud fraction) is the number of observed ECF $>$ 0.01 cases divided by the total number of observation with ECF retrieval. 19

3.2 Global distributions of filtered and gridded Aqua AIRS v6 L2 ice-phase (top), water-phase (middle), and unknown-phase (bottom) for vzenLow case for 2003 to 2012. The frequency is as defined in Equation 2.1. 21

3.3 Zonally averaged distributions of filtered and gridded Aqua AIRS ice- (top left), water- (top right), and unknown-phase (bottom) with respect to different vzen categories for 2003 to 2012. 22

3.4 Global distribution differences of filtered and gridded Aqua AIRS v6 L2 ice-phase (top), water-phase (middle), and unknown-phase (bottom) between vzenLow and vzenHigh cases for 2003 to 2012. 23

3.5 Zonally averaged distributions of filtered and gridded Aqua AIRS ice cloud optical thickness (left column) and ice cloud effective diameter (right column) for low (top row), middle (middle row), and high (bottom row) values for 2003 to 2012. 25

3.6 Cumulative distributions of filtered and gridded Aqua AIRS ice- (top left), water- (top right), and unknown-phase (bottom) with respect to different ECF categories for 2003 to 2012. 26

3.7 Global distribution differences of filtered and gridded Aqua AIRS v6 L2 ice-phase (top), water-phase (middle), and unknown-phase (bottom) between ECFLow and ECFHigh cases for 2003 to 2012. 28

3.8 Observation numbers of filtered and gridded Aqua AIRS v6 L2 ice-phases for different ECF cases from 2003 to 2012. P1, P2, P3, and P4 indicate cloud thermodynamic phase values of +1, +2, +3, and +4, respectively. Higher P values correspond to greater confidence in the ice phase classification. 29

3.9 Cumulative distributions of filtered and gridded Aqua AIRS ice cloud optical thickness (left) and ice cloud effective diameter (right) with respect to different ECF categories for 2003 to 2012. 29

3.10 Global distributions of single-layer (top) and two-layer (bottom) cloud cases from the Aqua AIRS data for 2003 to 2012. The layer definitions are summarized in Table 2.2. The sum of (SingleLayer) + (TwoLayer) = 1 for each grid cell. 30

3.11 Cumulative distribution of total cloud fraction with respect to different layer definitions summarized in Table 2.2. 31

3.12 Observation numbers of filtered and gridded Aqua AIRS v6 L2 cloud thermodynamic phase for different layer cases from 2003 to 2012. . . 32

3.13 Global distribution differences of filtered and gridded Aqua AIRS v6 L2 ice-phase (top), water-phase (middle), and unknown-phase (bottom) between two layer and single layer cases for 2003 to 2012. 33

3.14 Zonally averaged values (right) and cumulative distribution (left) of filtered and gridded Aqua AIRS ice cloud optical thickness with respect to different cloud layer definitions for 2003 to 2012. 34

3.15 Zonally averaged values (left column) and cumulative distributions (right column) of filtered and gridded Aqua AIRS ice cloud optical thickness for low (top row), medium (middle row), and high (bottom row) values for 2003 to 2012. 35

3.16 Zonally averaged values (right) and cumulative distribution (left) of filtered and gridded Aqua AIRS ice cloud effective diameter with respect to different cloud layer definitions for 2003 to 2012. 36

3.17 Zonally averaged values (left column) and cumulative distributions (right column) of filtered and gridded Aqua AIRS ice cloud effective diameter for low (top row), medium (middle row), and high (bottom row) values for 2003 to 2012. 37

3.18 Zonally averaged values of filtered and gridded Aqua AIRS upper layer cloud top temperature with respect to different viewing zenith angles for 2003 to 2012. Straight line indicates vzenLow, stars indicate vzenMid, and plus signs indicate vzenHigh. 38

3.19 Global distribution difference of filtered and gridded Aqua AIRS v6 L2 upper layer cloud top temperature between vzenLow and vzenHigh cases for 2003 to 2012. Cttall indicates no filtering applied to the retrieval. 39

3.20 Observation numbers of filtered and gridded Aqua AIRS v6 L2 cloud thermodynamic phase for different upper layer cloud top temperature regimes from 2003 to 2012. 39

3.21 Cumulative distribution of filtered and gridded Aqua AIRS upper layer cloud top temperature with respect to cloud thermodynamic phase for 2003 to 2012. 40

LIST OF TABLES

TABLE Page

2.1 Definition of variables and variable ranges based on the AIRS v6 Level 2 retrievals. 13

2.2 STG filtering parameters for AIRS v6 L2 data. 15

2.3 The total number of cloudy AIRS observations for vzenLow, vzenMid, and vzenHigh cases from 2003 to 2012. 16

3.1 Global average frequency differences of filtered and gridded Aqua AIRS v6 L2 ice-phase, water-phase, and unknown-phase between vzenLow and vzenHigh cases for different times of the year. 24

1. INTRODUCTION

While clouds play a vital role in the Earth's radiation budget and climate, they are still one of the largest uncertainties of the current climate models. According to the Intergovernmental Panel on Climate Change Fifth Assessment Report (IPCC AR5; Boucher et al., 2013), clouds apply an annual shortwave cloud radiative effect (SWCRE) of about -50 Wm^{-2} by contributing to planetary albedo, and apply a mean longwave cloud radiative effect (LWCRE) of about +30 Wm^{-2} by enhancing the greenhouse effect, globally. Therefore, clouds have a net cooling effect on the current climate with a net global mean cloud radiative effect (CRE) of -20 Wm^{-2}. Due to the key role of clouds, accurate parametrization of them is crucial to improving accuracies of climate models (Strabala et al., 1994). This is because a better understanding of clouds can decrease the uncertainty associated with them, such as the 10% range between reported estimates of LWCRE from satellite data (Loeb et al., 2009).

Some of the fundamental details of cloud microphysical processes, such as particle shape especially for ice- and mixed-phase clouds, are not well understood; hence, it is especially challenging to represent the microphysical processes in climate models (Boucher et al., 2013). While the accuracy of cloud climate projections has increased as more studies have been done, the uncertainty around clouds still poses a great problem in climate models (Stocker et al., 2013). For example, representations of cloud processes have been improved in global climate models employed in the Coupled Model Intercomparison Project - Phase 5 (CMIP5) relative to CMIP3 (Jiang et al., 2012). However, the CMIP5 model systematically overestimates cloud optical thickness and underestimates cloud fraction relative to satellite simulators with Cloud-Aerosol Lidar and Infrared Pathfinder Satellite Observations (CALIPSO), Po-

larization & Anisotropy of Reflectances for Atmospheric Sciences coupled with Observations from a Lidar (PARASOL), and Clouds and the Earths Radiant Energy System (CERES) observations (Nam et al., 2012).

Satellite observations are suitable data sets for comparing with model-derived cloud properties and to help diagnose problems in with modeled clouds. This is because large and statistically robust sets of observations for comparison are provided by satellites (Kahn et al., 2008), and are needed to evaluate model-simulated global cloud variables. According to Maddux et al. (2010), to understand the role of clouds in the Earth's radiation budget and climate, it is important to investigate the time and geographic regions clouds occur, and higher order properties of clouds. The needed global coverage at a sufficient temporal resolution for this investigation is only provided by satellite instruments (Maddux et al., 2010).

While satellite data is the primary global data for clouds, the fact that satellite retrievals are affected by artifacts, such as different cloud mask algorithms which distinguish clear pixels from cloudy ones, or resolution effects (Yang and Di Girolamo, 2008), may change the interpretation of satellite retrievals (Boucher et al., 2013). Since the definition of clouds depends on the sensitivity of satellites and on vertical overlap of cloud layers, it is not an easy task to compare model-simulated and satellite-derived cloud retrievals (Nam et al., 2012). For instance, depending on the viewing geometry, or the sensitivity of the instrument some clouds may be observed by some satellites while they are not by others (Bony et al., 2011). Norris (2011) compared cloud cover observations from the Extended Edited Cloud Report Archive (EECRA), which provides synoptic cloud reports from ships and land stations, to cloud cover observations obtained from the International Satellite Cloud Climatology Project (ISCCP), which uses data from NOAA, METEOSAT, GOES, and GMS satellites, and showed the existence of discrepancies in low-level cloud cover between

EECRA and ISCCP. According to Norris (2011), the presence of observational artifacts in ISCCP, such as a systematic dependence of cloud retrievals on view angle (Campbell, 2004), is a contributor to this discrepancy. In addition, Evan et al. (2007) demonstrated that the global decrease in cloud amounts exhibited by the ISCCP is due to non-physical satellite viewing angle geometry artifacts. To accurately use satellite cloud retrievals and avoid the non-physical influence of artifacts, satellite products have to be well understood. Therefore, it is important to investigate cloud retrievals from satellites and determine in which situations the retrievals are good and in which the retrieval algorithms may need refinements.

Wielicki et al. (1995) compiled a list of the cloud observations that are minimally required to monitor climate feedback of clouds and contribute to the representation of clouds in climate models. According to this study, when the development of a simple plane parallel layer cloud in a general circulation model (GCM) grid box over a dark ocean surface is considered, prediction of liquid water path (LWP) within the grid box is often the first step. Also, different cloud particle sizes will yield a range of cloud optical thickness values for the same LWP of water clouds. Since for a given optical thickness, particle size, and water mass, spherical water drops reflect less solar radiation than non-spherical ice particles (Kinne and Liou, 1989), cloud particle phase is also important. Additionally, cloud temperature, cloud height, and infrared emittance are required for calculation of longwave fluxes. Thus, particle phase and shape, visible optical thickness, particle size, fractional coverage, temperature and height, and infrared emittance are required parameters to observe climate feedback of clouds (Wielicki et al., 1995). Determination of cloud thermodynamic phase (ice, liquid water, or unknown phase) is not only one of the required retrievals, but also a necessary first step in retrieving cloud particle size, optical thickness, and water path (Nasiri and Kahn, 2008).

Microphysical properties of a cloud, such as effective size of particles, particle phase, and particle shape determine the cloud optical thickness and ice or liquid water path (Minnis et al., 1998). By governing the reflectance and emittance of clouds, these parameters importantly affect the radiation budget and climate (Minnis et al., 1998). Ice clouds affect the atmospheric energy budget through latent heat exchange, and by adjusting incoming and outgoing radiative energy (Minnis et al., 1993). While cirrus clouds are strong absorbers at infrared wavelengths, they absorb only part of the radiation emitted from the Earth's surface or lower levels because of their relatively small optical thicknesses (Minnis et al., 1993). Longwave radiation emission by high altitude ice clouds occurs at colder temperatures than the surface and lower atmospheric levels (Minnis et al., 1993). For example, the infrared radiance sensed by a satellite sensor neglecting scattering, which is depicted in Figure 1.1, is:

$$\begin{aligned} I(\lambda) &= I_1 + I_2 + I_3 + I_4 \\ &= \varepsilon_{s,\lambda} B_\lambda[T_s] t_\lambda(p_s)(1-\varepsilon_{c,\lambda}) \\ &+ (1-\varepsilon_{c,\lambda}) t_\lambda(p_c) \int_{p_s}^{p_c} B_\lambda[T(p)] \frac{dt(p)}{dp} dp \\ &+ \varepsilon_{c,\lambda} B_\lambda[T(p_c)] t_\lambda(p_c) \\ &+ \int_{p_c}^{0} B_\lambda[T(p)] \frac{dt(p)}{dp} dp \end{aligned} \tag{1.1}$$

where T_s indicates equivalent blackbody temperature of the surface, $\varepsilon_{s,\lambda}$ and $\varepsilon_{c,\lambda}$ are surface and cloud emissivities, respectively, $t_\lambda(p)$ is atmospheric transmissivity, p indicates pressure, and B_λ is the Planck function. When the statements made by both Wielicki et al. (1995) and Minnis et al. (1998) are considered, it is straightforward to see that cloud thermodynamic phase, ice cloud optical thickness, and ice cloud effective diameter affect the radiation budget.

Equation 1.1 shows the effects of transmissivity, emissivity, and equivalent black

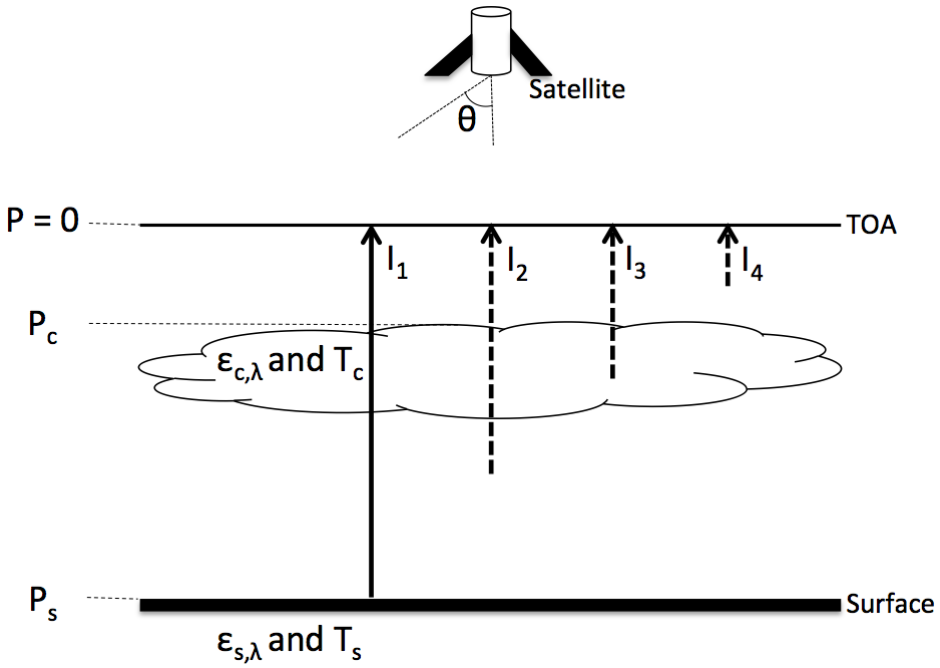

Figure 1.1: Illustration of cloudy sky infrared radiative transfer equation terms.

body temperature on the infrared radiance at the top of the atmosphere. The viewing zenith angle dependence of the infrared radiation at the top of the atmosphere is implicitly included in the transmissivity expression because of the definition of transmissivity, t = exp(-τ/cos(θ)) where τ indicates optical thickness and θ is viewing zenith angle. For example, an increase in viewing zenith angle causes longer optical paths; therefore, the contribution by surface radiation decreases and both attenuation and emission by cloud and atmospheric water vapor increase (Joyce et al., 2001). Cloud layering effect is also important because depending on the layering the effective emissivity of the cloudy scene changes, which directly impacts the radiation at the top of the atmosphere. Similarly, cloud fraction effects the retrievals. Given the same emissivity for a cloudy scene, the higher the cloud fraction (i.e., fraction of field of view covered by the cloud) is, the higher the spectral signature of the cloud is.

In addition, the time of the year changes cloud fraction, cloud top temperature, and cloudy emissivity. Thus, it is crucial to determine the effects of satellite's viewing zenith angle, cloud top temperature, cloud fraction, cloud layering, time of the year, or geographical region on satellite retrievals to gain an advanced understanding of satellite retrievals, such as cloud thermodynamic phase, cloud optical thickness and effective diameter, which affect the cloud radiation properties.

New and improved measurements of cloud properties, atmospheric temperature, atmospheric humidity, and land and ocean skin temperatures are provided by the Atmospheric Infrared Sounder (AIRS) / Advanced Microwave Sounding Unit (AMSU) data, with the accuracy, resolution, and coverage required by numerical weather prediction and climate models (Aumann et al., 2003). A list of important datasets that AIRS will contribute to climate studies is given by Aumann et al. (2003) as follows: atmospheric temperature profiles, sea-surface temperature, land-surface temperature and emissivity, relative humidity profiles and total precipitable water vapor, fractional cloud cover, cloud spectral infrared emissivity, cloud-top pressure and temperature, total ozone burden of the atmosphere, column abundances of minor atmospheric gases such as CO_2, CH_4, CO, and N_2O, outgoing longwave radiation and longwave cloud radiative forcing, and precipitation rate. The coincident data from the instruments is used to both improve and support climate related studies and numerical weather predictions, including the investigation of the potential correlation between cirrus clouds and global warming. AIRS observations are assimilated into for medium-range numerical weather prediction models. AIRS data is generally used for cloud related studies (Kahn et al., 2003; Nasiri and Kahn, 2008; Kahn et al., 2008; Jin, 2012; Jin and Nasiri, 2014).

The AIRS version 6 (v6) cloud products, released in April, 2013, are available for all 13 years of the AIRS data record. There are some significant changes between

the v5 and v6 cloud retrieval algorithms. Kahn et al. (2014) summarize the changes between AIRS v5 and v6 cloud retrieval algorithm and the way ice cloud properties are retrieved. One of the significant changes between v5 and v6 is that v6 provides retrievals, such as cloud temperature, within AIRS FOV which has a diameter of 13.5 km instead of the 45 km diameter AIRS/AMSU field of regard, which has an footprint of 3.3° and overlaps with nine of the AIRS FOVs with 1.1° footprints (Aumann et al., 2003). Also, a new set of cloud products added to the v6 support product files including cloud thermodynamic phase, ice cloud optical thickness (τ), ice cloud effective diameter (D_e), and ice cloud top temperature ($T_{C,ICE}$) (Kahn et al., 2014). AIRS v6 cloud thermodynamic phase retrieval algorithm described by Jin (2012) differentiates ice from liquid water based on thresholds of infrared brightness temperature (BT) and brightness temperature difference (BTD) tests which are only performed on AIRS pixels that have a retrieved effective cloud fraction of greater than 0.01. The new ice cloud property retrievals (τ and D_e) are simultaneously retrieved on individual AIRS FOVs containing ice-phase (Kahn et al., 2014).

Jin and Nasiri (2014) compared one year of AIRS infrared-based v6 cloud thermodynamic phase with the CALIPSO cloud thermodynamic phase and found that except for a larger discrepancy in high latitudes, over 90% of all ice detected as ice by CALIPSO are classified as ice by AIRS. While they concluded that the AIRS phase algorithm is effective at detecting ice clouds, they pointed out that refinements are needed to use the AIRS-detected water clouds because approximately 60% of water clouds fall into AIRS unknown phase. Because of CALIPSO's observational track through the AIRS granule, the Jin and Nasiri study only considered near-nadir AIRS data.

This study investigates AIRS v6 Level 2 (L2) cloud thermodynamic phase, ice cloud optical thickness, and ice cloud effective diameter to gain a better understand-

ing of the retrievals and to look for retrieval artifacts. In order to achieve this, the effects of satellite's viewing zenith angle, effective cloud fraction, two cloud layers, cloud top temperature, time of the year, and region on cloud thermodynamic phase, ice cloud optical thickness, and ice cloud effective diameter are investigated for ten years of AIRS v6 L2 support product data from 2003 to 2012. This study uses a uniform space-time gridding (STG) algorithm developed by Smith et al. (2013) to build globally gridded datasets of filtered AIRS v6 L2 ice cloud retrievals, which enhances user control over data filtering and ease comparisons with other instruments since it can be applied to data from any polar-orbiting or geostationary satellite.

The remainder of this thesis is organized as follows. Information about the AIRS instrument, the data used, and the STG algorithm are given in Chapter 2. In Chapter 3, the results are provided. Conclusions are given in Chapter 4.

2. DATA AND METHODS

2.1 The Atmospheric Infrared Sounder (AIRS) Version 6 Cloud Products

The Atmospheric Infrared Sounder (AIRS) instrument is designed to form an integrated cross-track scanning temperature and humidity sounding system with the Advanced Microwave Sounding Unit (AMSU) on the Aqua satellite of the Earth Observing System (EOS) (Aumann et al., 2003). The AIRS instrument is in a sun-synchronous orbit with an equatorial crossing local time of 01:30 in the descending and 13:30 in the ascending node (Kahn et al., 2014). AIRS was launched in May 2002. The instrument is an infrared spectrometer/radiometer which scans at angles $\mp 48.95^{\circ}$ from nadir and provides spectral coverage in the 3.74 - 4.61 m, 6.20 - 8.22 m, and 8.8 - 15.4 m infrared wavebands with 2378 channels at a nominal spectral resolution of $\lambda/\Delta\lambda = 1200$ (Aumann et al., 2003). The spatial resolution of AIRS at nadir view is 13.5 km, and there are nearly 2.9 million daily observations of field of views (FOVs) (Kahn et al., 2014). The AIRS version 6 cloud products, released in April, 2013, are available for all 13 years of the AIRS data record.

The new version 6 (v6) cloud retrieval algorithm uses nine individual retrievals in the AMSU field of regard (FOR) (Figure 2.1, dashed circle in the upper right corner) and four parameters are retrieved for every AIRS FOV (Figure 2.1, solid circles in the upper right corner) (Kahn et al., 2014). These include up to two layers of both cloud top temperature (T_C) and effective cloud fraction (ECF) (Kahn et al., 2014). Therefore, unlike the version 5 (v5) that provides T_C within AIRS/AMSU FOR with a diameter of 45 km, T_C is provided within every AIRS FOV which has a diameter of 13.5 km. ECF which is the multiplication of spatial cloud fraction and cloud emissivity (i.e., the value of cloud fraction if the emissivity were always one) and

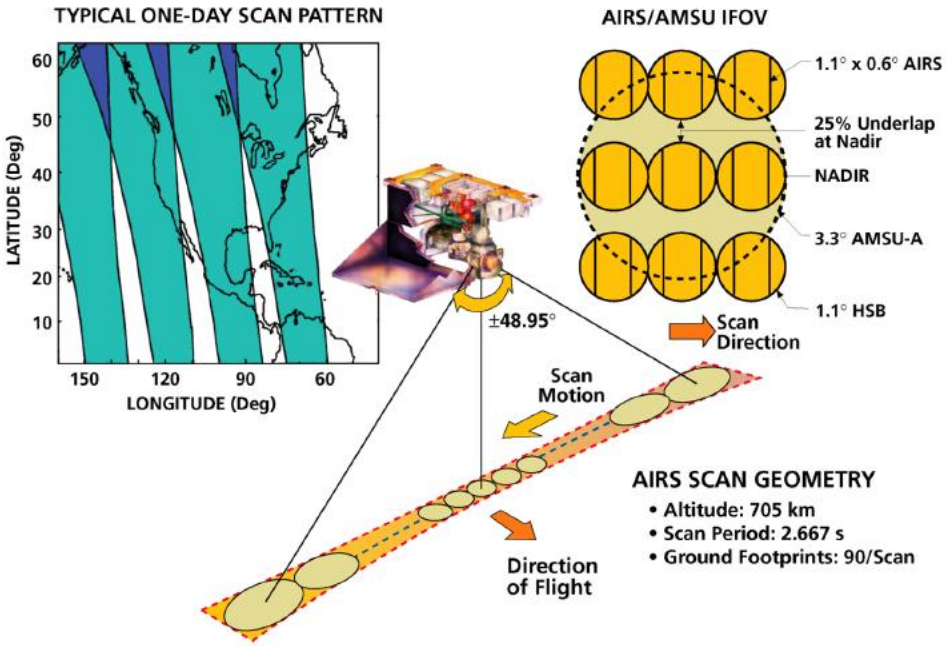

Figure 2.1: Scan geometry of AIRS/AMSU at nadir view. Solid circles and dashed circle in the upper right corner indicate AIRS FOV and AMSU FOR, relatively. This figure is adapted from Aumann et al. (2003).

T_C are retrieved upon completion of a cloud-clearing methodology determined by Susskind et al. (2003) (Kahn et al., 2014). In addition, a new set of cloud products was added to the v6 support product files including cloud thermodynamic phase, ice cloud optical thickness (τ), ice cloud effective diameter (D_e), and ice cloud top temperature ($T_{C,ICE}$) (Kahn et al., 2014).

AIRS v6 cloud thermodynamic phase retrieval algorithm described by Jin (2012) and Jin and Nasiri (2014) differentiates ice from liquid water based on thresholds of brightness temperature (BT) and brightness temperature difference (BTD) tests. The main objective of the algorithm is to find as many ice clouds as possible since high level clouds and upper portions of opaque clouds significantly contribute to

AIRS top of the atmosphere radiances (Jin, 2012). The BT and BTD tests are only performed on AIRS pixels that have a retrieved effective cloud fraction of greater than 0.01. There are four different ice-phase tests: (1) BT at 960 cm^{-1} < 235 K; (2)

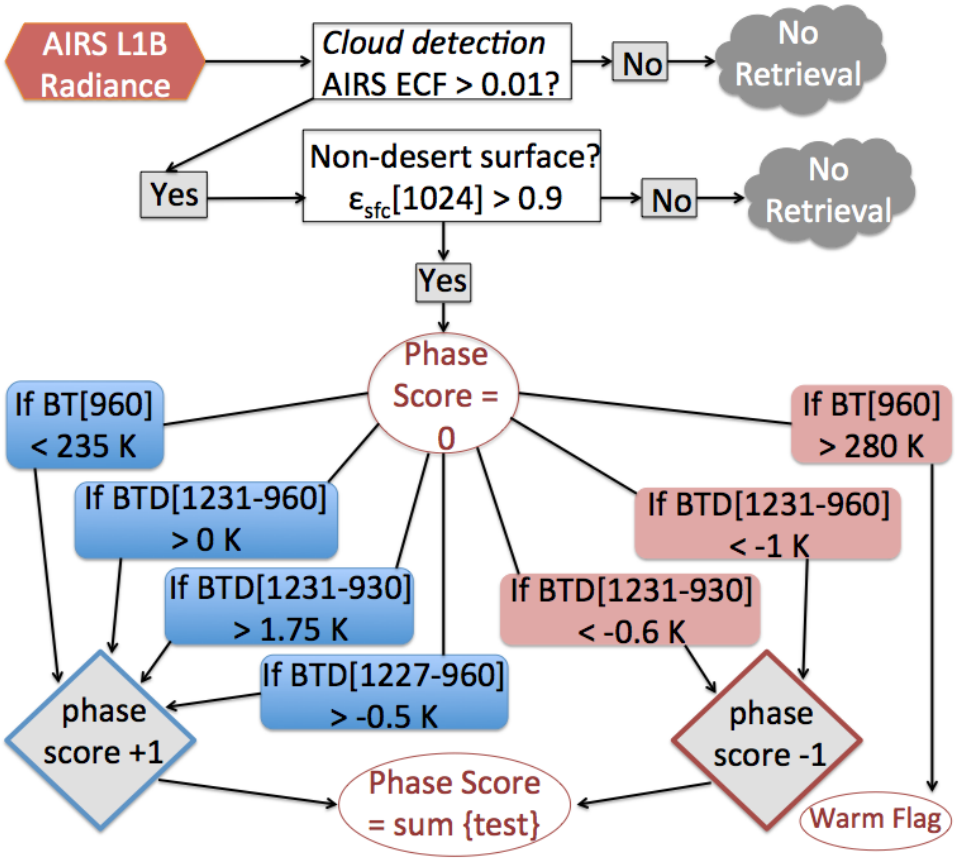

Figure 2.2: Schematic view of AIRS cloud thermodynamic phase.

BTD between 1231 and 960 cm^{-1} ($BTD_{1231-960}$) > 0.0 K; (3) BTD between 1231 and 930 cm^{-1} ($BTD_{1231-930}$) > 1.75 K; and (4) BTD between 1227 and 960 cm^{-1} ($BTD_{1227-960}$) > -0.5 K. In addition, there are two different liquid water-phase tests: (1) BTD between 1231 and 960 cm^{-1} ($BTD_{1231-960}$) < -1.0 K; (2) BTD between 1231 and 930 cm^{-1} ($BTD_{1231-930}$) < -0.6 K. There is an additional warm scene only

test, BT at 960 cm^{-1} > 280 K, which is not used in the final phase determination. For each of the ice (liquid water) tests passed, the algorithm assigns a phase score of +1 (-1). Then, the phase scores for all tests passed are summed and the final phase score is determined.

According to the result of this summation, scenes are classified as ice if the phase score sum has a value from +1 to +4, liquid water if the sum has a value of -2 or -1, or unknown if the sum is 0. The greater the positive value from 1 to 4 is, the higher the confidence that the cloud is in the ice phase. The lower negative values from -1 to -2 indicate that the cloud is in the liquid water phase with an higher confidence. The unknown category means either no test passes or one or two ice and liquid water tests pass simultaneously, canceling each other. Jin and Nasiri (2014) showed that over 99% of unknown do not pass ice or liquid tests. Figure 2.2 provides a flowchart of the algorithm. The AIRS cloud thermodynamic phase retrieval has the same resolution as the AIRS level-1B radiances and is located in the v6 L2 Support files (Kahn et al., 2014). Table 2.1 shows the abbreviations for the AIRS cloud thermodynamic phase retrievals used in this study.

The new v6 ice cloud property retrievals, τ which is inferred at 0.55 μm and D_e, are retrieved in log space to avoid negative values and they are simultaneously retrieved with $T_{C,ICE}$ on individual AIRS FOVs containing ice meaning the FOVs in which +1 to +4 tests passed (Kahn et al., 2014). τ and D_e are retrieved upon the completion of the AIRS Standard L2 retrieval using an optimal estimation algorithm derived from the Tropospheric Emission Spectrometer (TES) retrieval (Bowman et al., 2006). τ and D_e retrievals include quality control (QC) indicators. For τ, QC ranges from 0 to 2, and only 1 and 2 values are available for D_e, where 0 indicates "best", 1 indicates "good", and 2 indicates "do not use" (Kahn et al., 2014). Kahn et al. (2014) discourage the use of QC = 2 scenes except by the expert

Table 2.1: Definition of variables and variable ranges based on the AIRS v6 Level 2 retrievals.

Cloud Phase	
cldPhaseIce	$1 \leq$ cldPhase ≤ 4
cldPhaseWat	-2 $\leq$ cldPhase $\leq$ -1
cldPhase0	cldPhase = 0
cldPhaseM2	cldPhase = -2
cldPhaseM1	cldPhase = -1
cldPhaseP1	cldPhase = 1
cldPhaseP2	cldPhase = 2
cldPhaseP3	cldPhase = 3
cldPhaseP4	cldPhase = 4

Optical Thickness	
TauLow	$0 \leq \tau \leq 1$
TauMid	$1 < \tau \leq 2.5$
TauHigh	$2.5 < \tau \leq 8$

Effective Diameter (μm)	
DeLow	$0 \leq D_e \leq 40$
DeMid	$40 < D_e \leq 52$
DeHigh	$52 < D_e \leq 100$

user; therefore, scenes with QC = 2 are omitted. τ and D_e are located in the v6 L2 Support product files. In this study, to make detailed investigations, both τ and D_e are divided into three bins by considering nearly equal sample sizes for the bins, which are summarized in Table 2.1.

2.2 Uniform Space-Time Gridding Algorithm

This study relies on the space-time gridding (STG) approach developed by Smith et al. (2013) to build globally gridded datasets of filtered AIRS version 6 Level 2 ice cloud products. The STG algorithm can be applied to Level 2 products of any polar-orbiting or geostationary satellite to create daily gridded datasets. Then, longer time-averaged datasets can be created by averaging the daily grids. The STG consists of two components which are space gridding and time gridding.

In the space-gridding phase, satellite products are projected to a uniform n° x n° equal-angle grid (n > 0) from their instrument grid. In this phase, users can set general filtering parameters such as grid size, maximum latitude, maximum solar zenith angle, and maximum viewing zenith angle. The ability to set these parameters

provides the opportunity to investigate specifically desired scenes. For example, by appropriately setting up the maximum latitude filter, a user can look at only tropical data or by setting the maximum solar zenith angle $< 90^{\circ}$ filtering parameter, the user can focus on only daytime data. Once these parameters are set, observations are gathered into nearest-neighbor sets according to the specified grid cell size. Unlike the conventional nearest-neighbor approach that assigns each grid cell to its nearest neighbor observation, this method assigns each observation to its nearest neighbor grid cell so that sample size is at least one. By discarding the data that is not included by the filtering process, a data reduction is applied, which speeds up the time gridding portion of the algorithm.

The second phase of the STG algorithm is time gridding where daily statistics per grid cell are created. In this phase, observations from different times of the day, which are clustered into nearest neighbor sets per grid cell during the first phase, are statistically summarized into a single daily value. Measurements that have a number of observations greater than zero in each grid cell are averaged to create one mean daily value per grid cell. Then, the daily calculated grids can be aggregated to generate averaged datasets of a longer time such as a month, a season, or a year.

2.2.1 STG algorithm application

In this study, the STG algorithm is used to filter and grid Aqua AIRS v6 L2 cloud thermodynamic phase, ice cloud optical thickness, and effective diameter from 2003 to 2012. Table 2.2 summarizes the grid size and the filtering parameters used.

The grid size for the space gridding part is determined as 2° x 2° since this resolution is similar to the ones used in climate models. The satellite viewing zenith angle (vzen) filter consists of three parts (Table 2.2). The vzenLow case is considered as the reference point since the Jin and Nasiri AIRS study was based on comparisons

with CALIPSO and CALIPSO-AIRS collocations only occur for near-nadir AIRS scenes. Since AIRS cloud thermodynamic phase retrievals are only valid for pixels that have an ECF greater than 0.01, ECF values smaller than 0.01 are not considered. Cloud top temperature used is the standard L2 upper level cloud top temperature (ctt). This retrieval represents the cloud layer if the scene is a single layer scene, or the upper layer in the case of two layers. To investigate the effect of cloud layering

Table 2.2: STG filtering parameters for AIRS v6 L2 data.

Grid Size	2° x 2°		
Viewing Zenith Angle		**Effective Cloud Fraction**	
vzenLow	$0^\circ < \mid \text{vzen} \mid \leq 27^\circ$	*ECFLow*	$0.01 \leq \text{ECF} \leq 0.1$
vzenMid	$27^\circ < \mid \text{vzen} \mid \leq 38^\circ$	*ECFMid*	$0.1 < \text{ECF} \leq 0.6$
vzenHigh	$38^\circ < \mid \text{vzen} \mid \leq 48^\circ$	*ECFHigh*	$0.6 < \text{ECF} \leq 1.0$
Cloud Top Temperature		**Layering**	
cttLow	$\text{ctt} < 243$ K	*SingleLayer*	LCF $\leq$ 0.1*UCF
cttMid	$243 \leq \text{ctt} < 273$ K	*TwoLayer*	LCF > 0.1*UCF
cttHigh	$\text{ctt} \geq 273$ K		

on the ice cloud retrievals, two different layer definitions are made. SingleLayer case indicates scenes where lower cloud fraction (LCF) is either equal to or smaller than 10% of the upper cloud fraction (UCF) among the scenes with ECF $\geq$ 0.01. TwoLayer represents scenes where lower cloud fraction (LCF) is greater than 10% of the upper cloud fraction (UCF) with an ECF greater than 0.01.

A minimum number of daily observations threshold is applied to ensure a statistically robust sample size for a grid cell. According to this threshold, grid cells which contain number of observations lower than 3.5% - half of 1.5 standard deviation - of

the mean number of observations aggregated in a year are not considered. Therefore, only the grid cells having a significant amount of daily observed pixels are used to calculate the averages.

Table 2.3 shows the total number of cloudy observations for different vzen categories for a ten year period from 2003 to 2012 of AIRS v6 L2 data. 55.6%, 27.7%,

Table 2.3: The total number of cloudy AIRS observations for vzenLow, vzenMid, and vzenHigh cases from 2003 to 2012.

	Total numbers x 10^9
vzenLow	5.5777 (55.6%)
vzenMid	2.7820 (27.7%)
vzenHigh	1.6754 (16.7%)

and 16.7% of the total observations fall into the vzenLow, vzenMid, and vzenHigh categories, respectively. While the number of observations for each category are different, frequency distributions which are investigated with respect to each category are not directly affected by this difference. This is because the frequency definition in Equation 2.1 gives relative frequency for each category:

$$f_{i,j} = \frac{cobs_{i,j}}{tobs_i} \tag{2.1}$$

where i represents the category of interest (i.e., vzenLow), j indicates the retrieval of interest (i.e., cldPhaseIce), $\text{cobs}_{i,j}$ gives the number of retrieval j for the category i (i.e., number of ice-phase retrievals for vzenLow category), and tobs_i indicates the total number of observations for the category i (i.e., the total number of observations with cloud phase retrievals for vzenLow).

Figure 2.3 gives the fractions of ECFLow, ECFMid, and ECFHigh categories out of all cases with ECF retrievals. ECFLow cases mostly occur over tropical and subtropical oceanic areas. The majority of clouds are contained within the ECFMid category. In addition, ECFHigh category is most common in ice cloud regions, such as the Inter Tropical Convergence Zone (ITCZ), tropical South America, Maritime Continent, and Central Africa, and in marine stratus and stratocumulus regions, high latitude oceanic areas, and over mountainous areas, such as the Tibetan Plateau and the west North America.

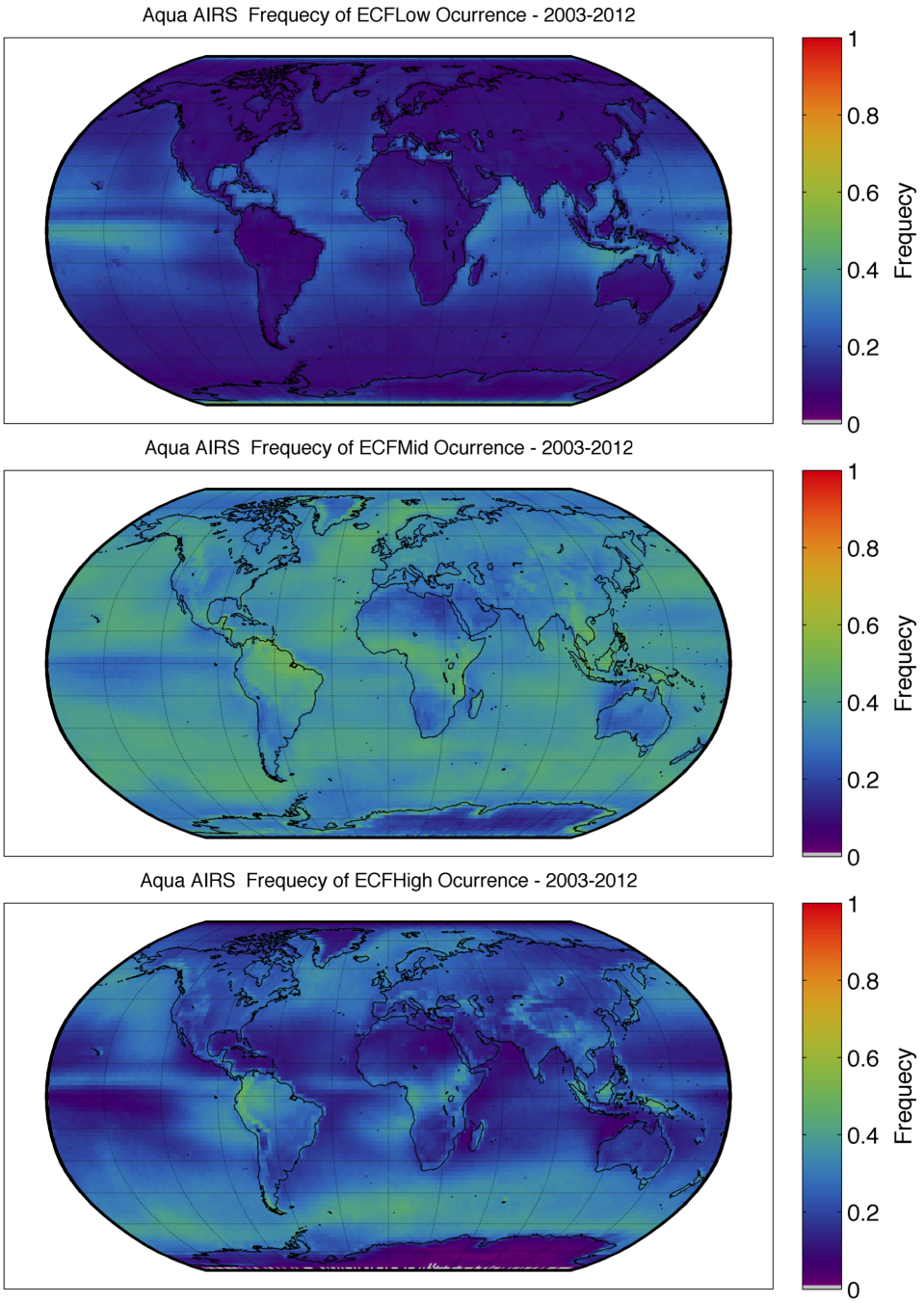

Figure 2.3: Global distributions of filtered and gridded Aqua AIRS v6 L2 ECFLow (top), ECFMid (middle), and ECFHigh (bottom) for 2003 to 2012. The frequency is the number of observed ECFLow, ECFMid, or ECFHigh divided by the total number of observation with ECF retrieval.

3. RESULTS

Aqua AIRS version 6 (v6) Level 2 (L2) cloud products for the years 2003 - 2012 are investigated by using the space-time gridding (STG) algorithm. Figure 3.1 shows

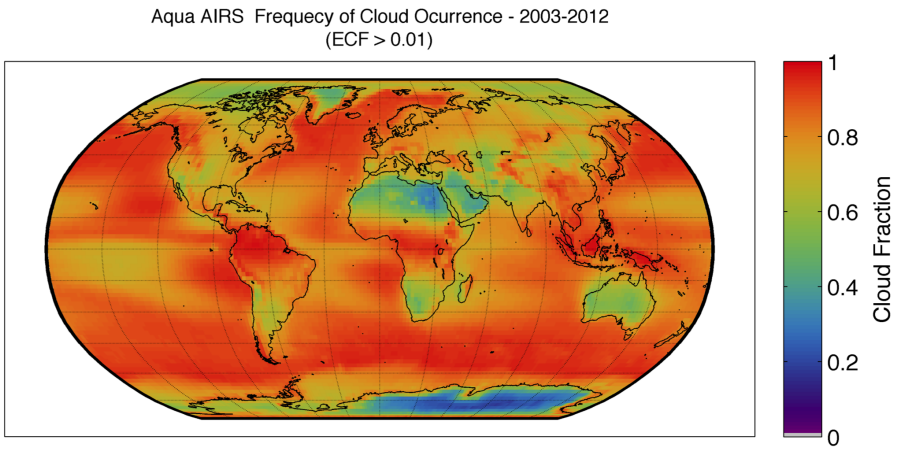

Figure 3.1: Global distribution of filtered and gridded Aqua AIRS v6 L2 cloud fraction for 2003 to 2012. The frequency (cloud fraction) is the number of observed ECF > 0.01 cases divided by the total number of observation with ECF retrieval.

the global cloud fraction distribution for ten years of AIRS v6 L2 data. Regions with highest frequencies of cloud occurrence correspond to those which are summarized for ECFHigh category in the previous section (Figure 2.3). The distribution provided in Figure 3.1 is similar, with slightly higher magnitudes, to those given by IPCC AR5 from CloudSat/CALIPSO 2B-GEOPROF-LIDAR data set for 2006 to 2011 (Boucher et al., 2013), by Wylie et al. (2005) from the High Resolution Infrared Radiometer Sounder (HIRS) data for 1979 to 2001, and by Kahn et al. (2014) from AIRS data for 2007. The differences in cloud fractions can be explained by different filtering approaches among studies mentioned, different pixel sizes used, and sensitivities of

individual instruments and algorithms.

Figure 3.2 shows the global distributions of AIRS ice-, water-, and unknown-phase for the years 2003 - 2012 for vzenLow category. Ice-phase frequencies are highest over the Maritime Continent, the Inter Tropical Convergence Zone (ITCZ), central Africa, and the north parts of South America. Water-phase frequencies are the highest in marine stratus and stratocumulus regimes over west of California, South America, South Africa, and Australia. The distributions of ice- and water-phase provided in Figure 3.2 are similar to those provided by Lin et al. (2010) from the Clouds and the Earth's Radiant Energy System (CERES) - MODIS data for 2005 and by Kahn et al. (2014) from AIRS data for 2007. Also, the unknown-phase distribution in Figure 3.2 which is similar to the one provided by Kahn et al. (2014) from AIRS data for 2007 shows that the unknown category appears to be robustly detecting trade cumulus clouds.

3.1 Satellite's Viewing Zenith Angle Effect

The effects of satellite's viewing zenith angle (vzen) on AIRS cloud thermodynamic phase, ice cloud optical thickness (τ), and ice cloud effective diameter (D_e) are investigated. Figure 3.3 provides the zonally averaged cloud thermodynamic phase frequencies with respect to different vzens which are summarized in Table 2.2 (vzenLow: $0^\circ < |\text{vzen}| \leq 27^\circ$; vzenMid: $27^\circ < |\text{vzen}| \leq 38^\circ$; vzenHigh: $38^\circ < |\text{vzen}| \leq 48^\circ$). According to this figure, vzen has little effect on zonally averaged ice-phase detection. On the other hand, higher vzens lead to more water and fewer unknown retrievals. The effect of vzen is the greatest in the mid-latitudes. Figure 3.4 shows the global distribution differences between vzenLow and vzenHigh cases for Aqua AIRS cloud thermodynamic phase. This figure is another indication of the vzen effect on AIRS-phase, especially on water- and unknown-phase. In mountain-

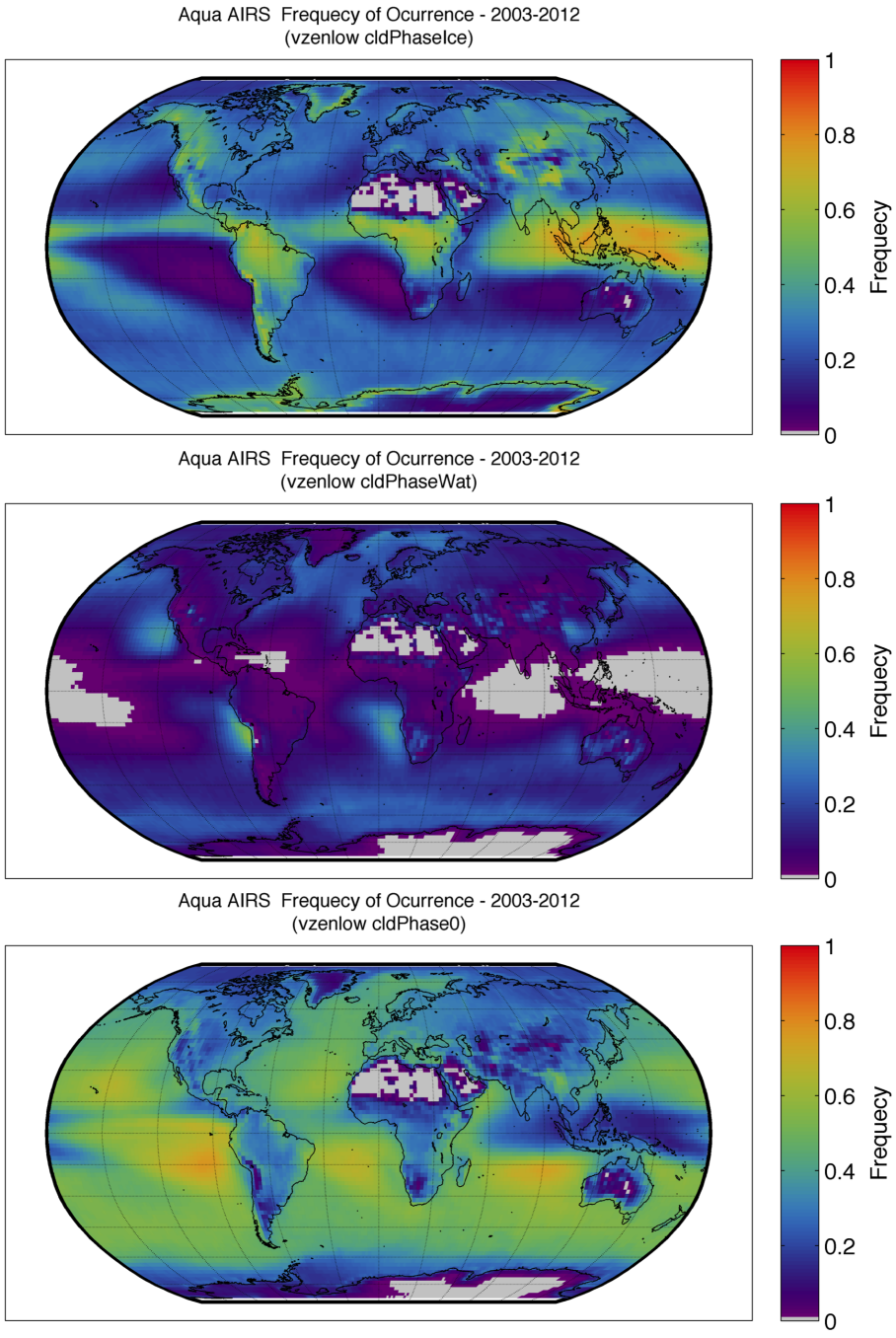

Figure 3.2: Global distributions of filtered and gridded Aqua AIRS v6 L2 ice-phase (top), water-phase (middle), and unknown-phase (bottom) for vzenLow case for 2003 to 2012. The frequency is as defined in Equation 2.1.

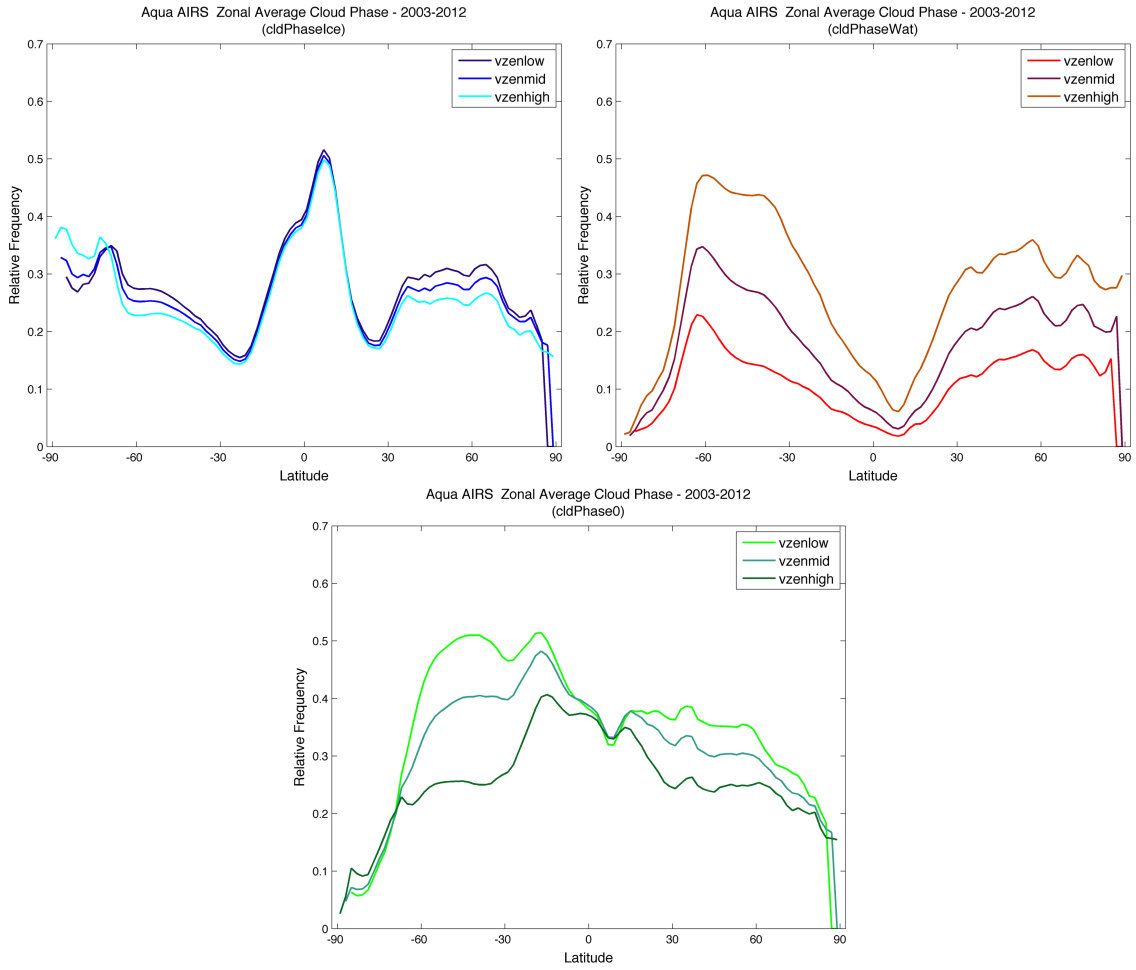

Figure 3.3: Zonally averaged distributions of filtered and gridded Aqua AIRS ice- (top left), water- (top right), and unknown-phase (bottom) with respect to different vzen categories for 2003 to 2012.

ous areas, such as the Tibetan Plateau and the west North America, higher vzens yield fewer ice and more unknown-phase pixels. Low surface temperatures of these areas and surface emissivity issues regarding these unvegetated areas play a role on the difference. The highest differences for water- and unknown-phase pixels between vzenLow and vzenHigh cases occur in the stratus and stratocumulus regions where water-phase fractions appear the highest in Figure 3.2. Kahn et al. (2011) showed that heterogeneity increases as vzen increases, which may decrease the ability of the

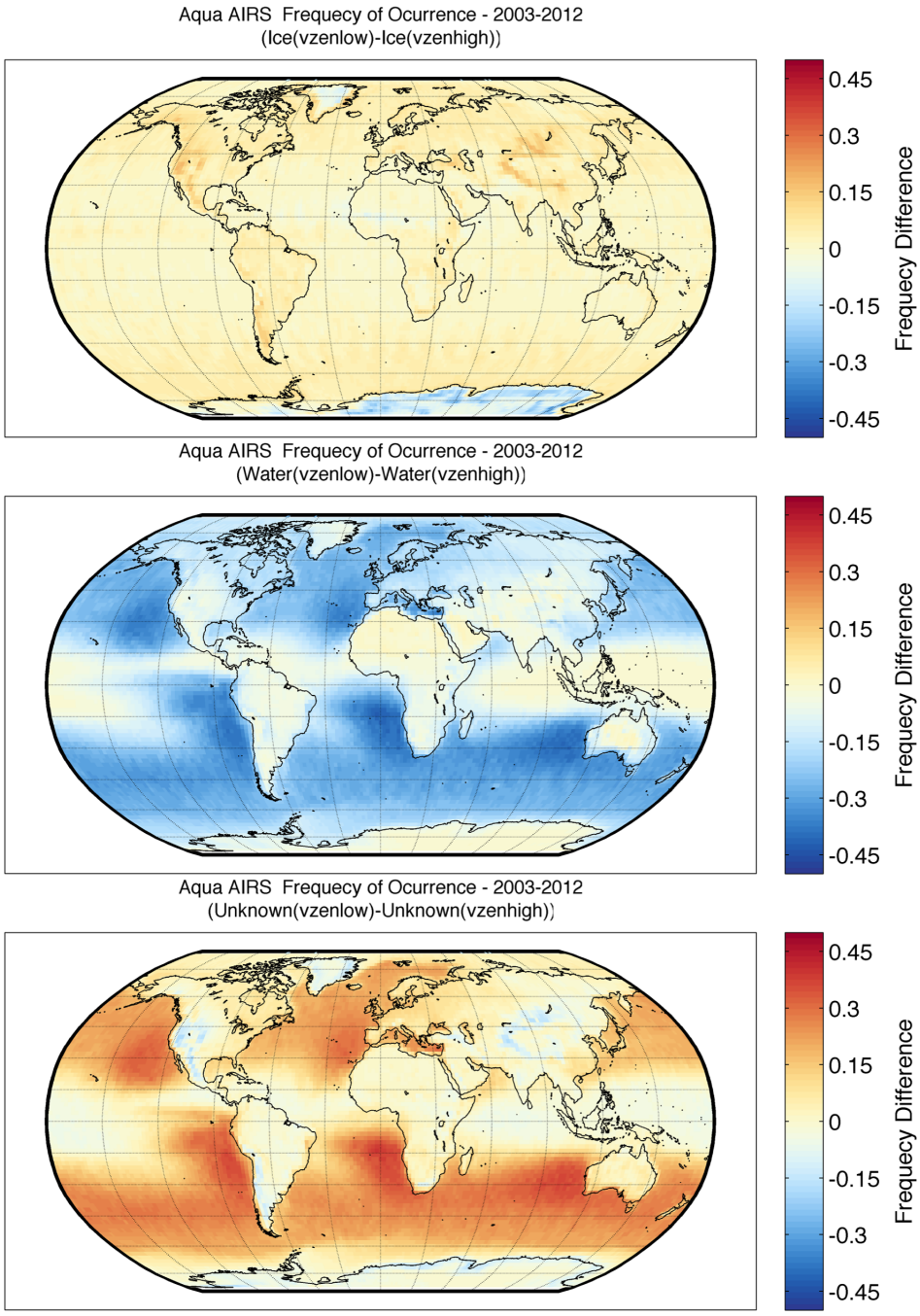

Figure 3.4: Global distribution differences of filtered and gridded Aqua AIRS v6 L2 ice-phase (top), water-phase (middle), and unknown-phase (bottom) between vzenLow and vzenHigh cases for 2003 to 2012.

algorithm to classify cloud phase. This may explain why the frequency distributions change as vzen deviates from near nadir.

Table 3.1 gives the differences between vzenLow and vzenHigh cases of global average distributions of AIRS-phase for December - January - February (DJF) and March - April - May (MAM) from 2003 to 2013, June - July - August (JJA) from 2003 to 2012, and September - October - November (SON) from 2002 to 2012. Table 3.1 shows that the vzen dependence of AIRS-phase is not strongly affected by the time of the year on a global scale.

Table 3.1: Global average frequency differences of filtered and gridded Aqua AIRS v6 L2 ice-phase, water-phase, and unknown-phase between vzenLow and vzenHigh cases for different times of the year.

	ice	water	unknown
DJF	0.02	-0.16	0.10
MAM	0.02	-0.15	0.09
JJA	0.02	-0.17	0.11
SON	0.02	-0.18	0.12

The vzen effect is also investigated for τ and D_e retrievals. Figure 3.5 gives the zonally averaged low, middle, and high τ and D_e values with respect to different vzen cases. Figure 3.5 indicates that retrieved τ and D_e show a weak dependence on vzen. Low, middle, and high values of τ tend to be greater as vzen gets higher.

3.2 Effective Cloud Fraction Effect

Aqua AIRS cloud thermodynamic phase, τ, and D_e are also investigated with respect to effective cloud fraction (ECF). Figure 3.6 shows the cumulative distribution functions of ice, water, and unknown AIRS-phases with respect to three differ-

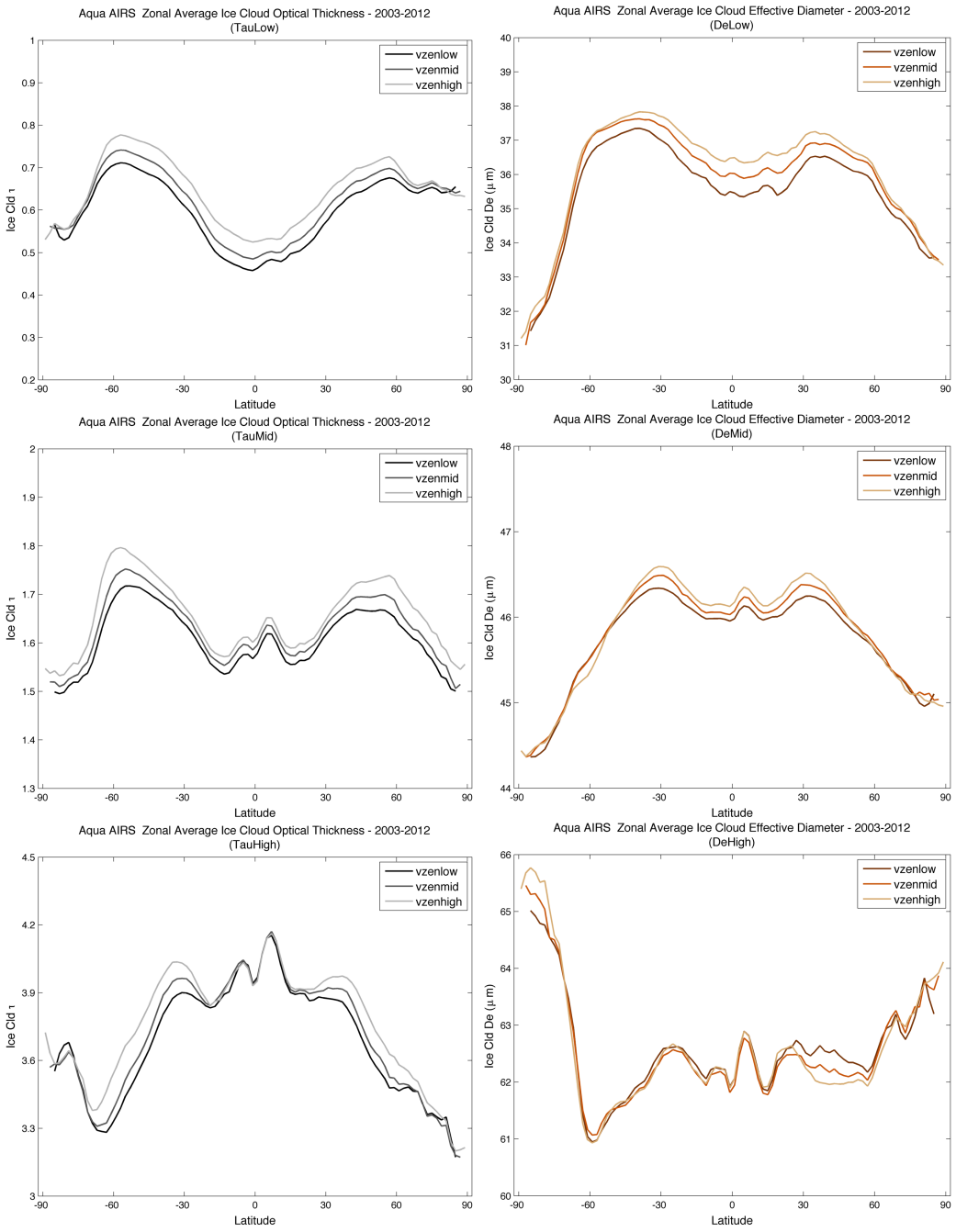

Figure 3.5: Zonally averaged distributions of filtered and gridded Aqua AIRS ice cloud optical thickness (left column) and ice cloud effective diameter (right column) for low (top row), middle (middle row), and high (bottom row) values for 2003 to 2012.

ent ECF cases which are summarized in Table 2.2 (ECFLow: $0.01 \leq \text{ECF} \leq 0.1$; ECFMid: $0.1 < \text{ECF} \leq 0.6$; ECFHigh: $0.6 < \text{ECF} \leq 1.0$). Figure 3.6 shows that ice- and water-phase frequencies increase as the ECF increases, and unknown-phase frequency decreases. Figure 3.7 shows the global distribution differences between

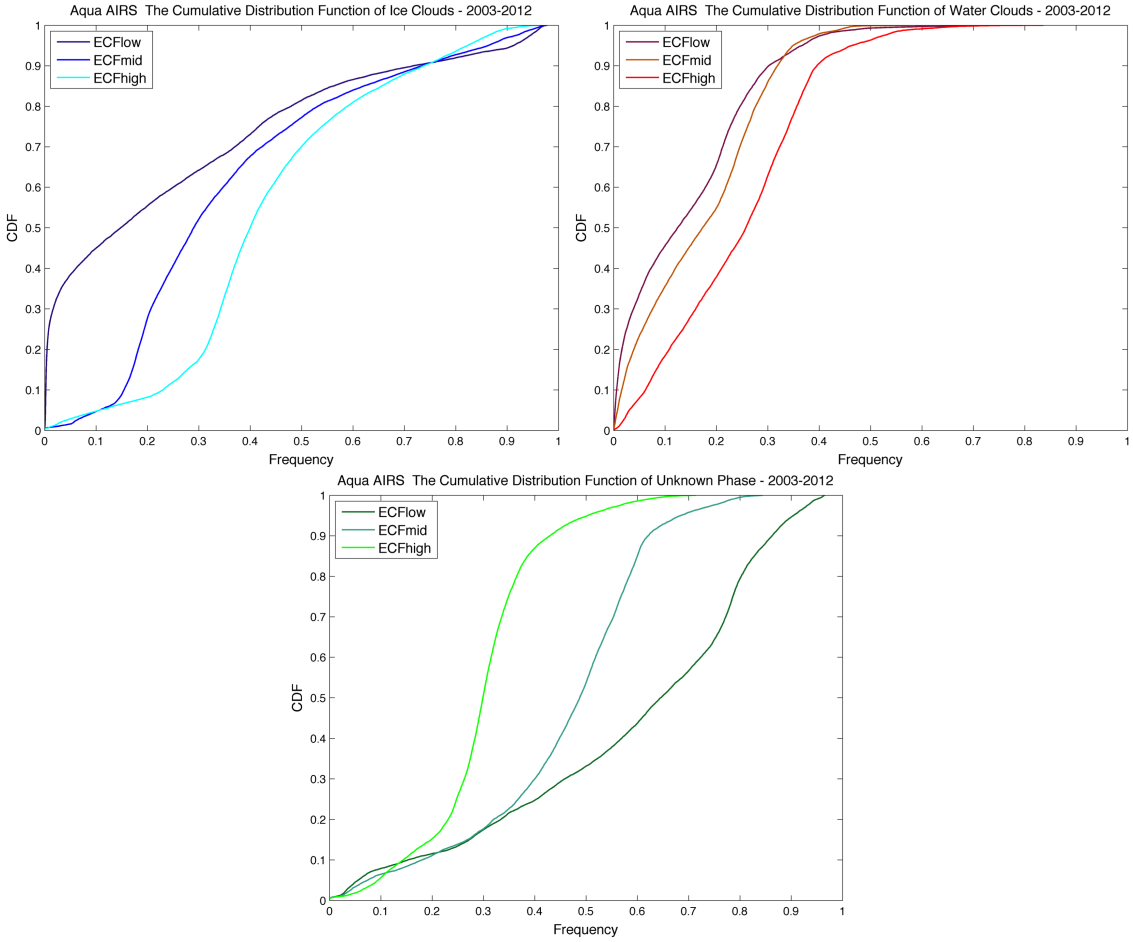

Figure 3.6: Cumulative distributions of filtered and gridded Aqua AIRS ice- (top left), water- (top right), and unknown-phase (bottom) with respect to different ECF categories for 2003 to 2012.

ECFLow and ECFHigh cases for Aqua AIRS cloud thermodynamic phase. This figure also shows that higher ECF leads to fewer unknown-phase retrievals, and more

ice- and water-phase retrievals. The distribution differences in Figure 3.7 show that ice (water) phase frequencies increase in ice (water) cloud regimes from Figure 3.2, and unknown phase frequency decreases globally. Therefore, it can be concluded that the phase detection ability of the algorithm increases with ECF. This is because ECF is a combination of spatial cloud fraction and cloud emissivity (i.e., spatial cloud fraction x cloud emissivity) (Kahn et al., 2008) within the AIRS field of view. Thus, for the same cloud emissivity, the phase signature is greater for higher spatial cloud fraction.

The numbers of observations for each individual ice-phase from +1 to +4 with respect to different ECF cases are given in Figure 3.8. Since greater positive values from 1 to 4 of AIRS-phase correspond to higher confidence that the cloud is in the ice phase, Figure 3.8 shows that higher ECFs correlate with greater ice-phase confidence. This is partly because one of the phase tests depends on the brightness temperature (BT) at 960 cm^{-1}; the BT at 960 cm^{-1} < 235 K test, is only true for high effective cloud fraction because cloud temperature is essentially equivalent to cloud brightness temperature for optically thick clouds with high emissivity.

The cumulative distribution functions of τ and D_e with respect to different ECF cases are given in Figure 3.9. Higher ECFs correspond to greater values of τ. For example, ~90% of τ points have values between 1.38 and 3.49, 0.71 and 1.25, and 0.17 and 0.80 for ECFHigh, ECFMid, and ECFLow cases, respectively. This is because higher τ means higher emissivity (i.e., in the absence of scattering, $\varepsilon \sim (1 - e^{-\tau})$) which, in turn, leads to higher ECF. While the effect of ECF on D_e is not as strong as it is on τ, according to Figure 3.9, higher ECFs lead to slightly greater D_e values.

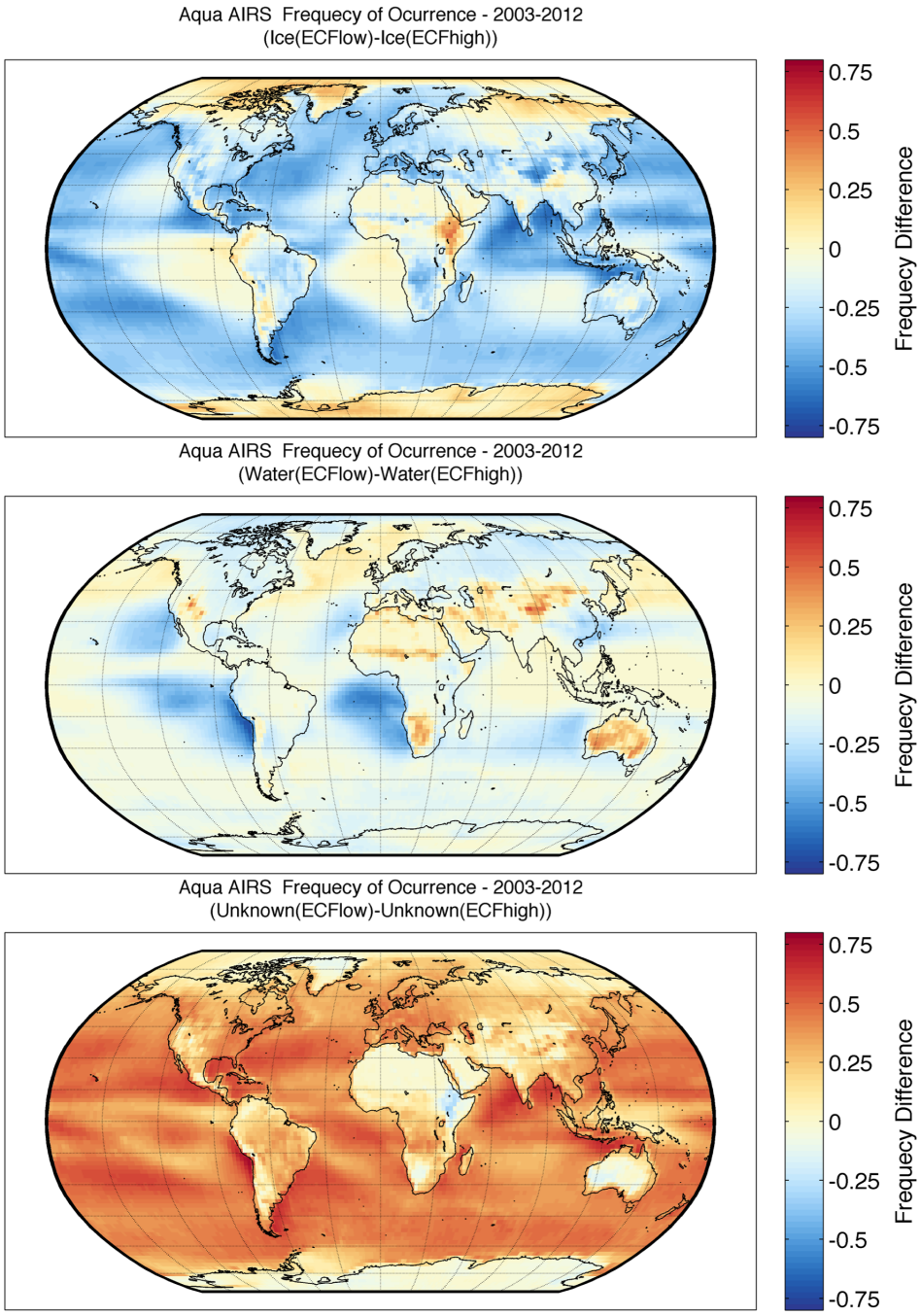

Figure 3.7: Global distribution differences of filtered and gridded Aqua AIRS v6 L2 ice-phase (top), water-phase (middle), and unknown-phase (bottom) between ECFLow and ECFHigh cases for 2003 to 2012.

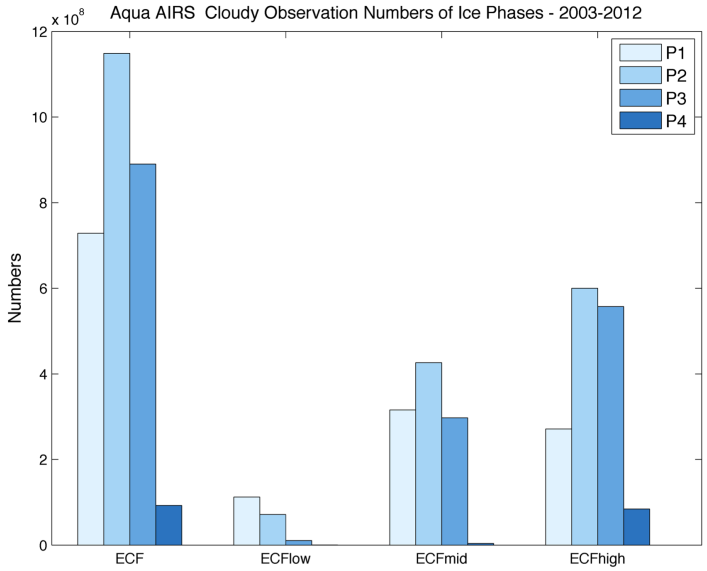

Figure 3.8: Observation numbers of filtered and gridded Aqua AIRS v6 L2 ice-phases for different ECF cases from 2003 to 2012. P1, P2, P3, and P4 indicate cloud thermodynamic phase values of +1, +2, +3, and +4, respectively. Higher P values correspond to greater confidence in the ice phase classification.

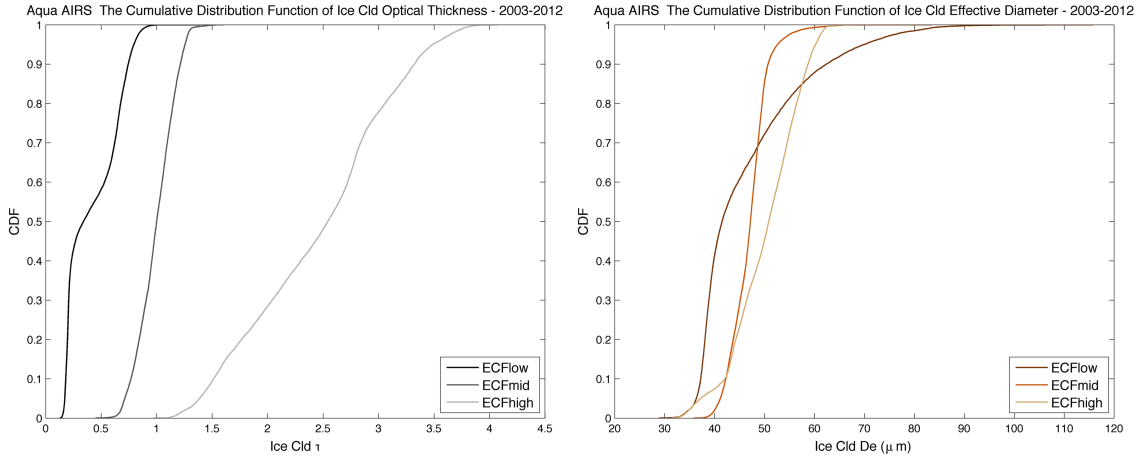

Figure 3.9: Cumulative distributions of filtered and gridded Aqua AIRS ice cloud optical thickness (left) and ice cloud effective diameter (right) with respect to different ECF categories for 2003 to 2012.

3.3 Cloud Layering Effect

The effects of cloud layering on Aqua AIRS cloud thermodynamic phase, τ, and D_e are investigated using the layer definitions summarized in Table 2.2. Figure 3.10 shows the global frequency distributions of single layer and two layer cloud cases. According to this figure, except the near-pole regions of Southern and Arctic Oceans,

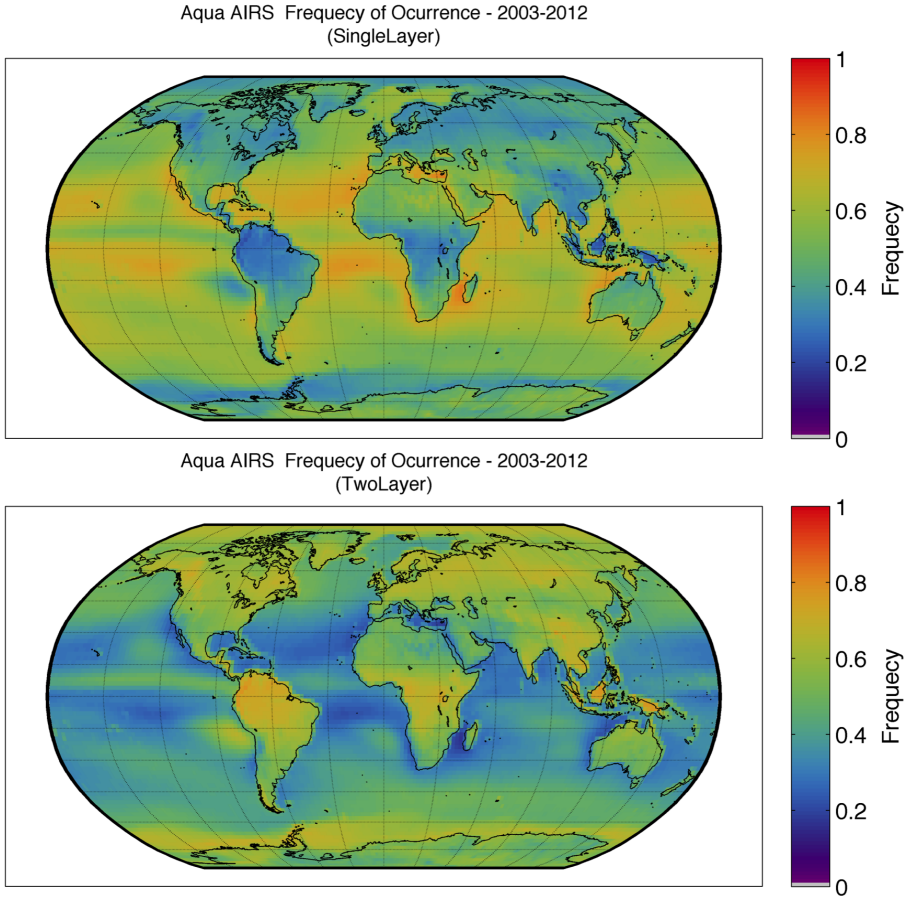

Figure 3.10: Global distributions of single-layer (top) and two-layer (bottom) cloud cases from the Aqua AIRS data for 2003 to 2012. The layer definitions are summarized in Table 2.2. The sum of (SingleLayer) + (TwoLayer) = 1 for each grid cell.

single-layer cases which indicate the scenes with a lower cloud fraction being either equal to or smaller than 10% of the upper cloud fraction occur more frequently over oceans while two-layer cases are more frequent over lands. Figure 3.11 shows the cumulative distribution function of the total cloud fraction with respect to different layer definitions. ∼90% of total cloud fraction values are between 0.25 and 0.61 for single-layer case and ∼90% of total cloud fraction values are between 0.38 and 0.76 for two-layer category. Therefore, two cloud layer scenes are generally associated with greater total cloud fractions than single-layer cloud scenes are.

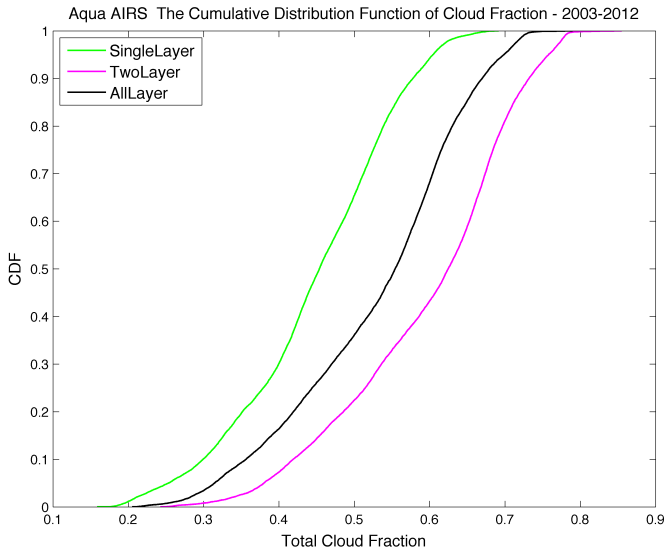

Figure 3.11: Cumulative distribution of total cloud fraction with respect to different layer definitions summarized in Table 2.2.

Figure 3.12 shows the numbers of cloudy observations of Aqua AIRS ice-, water-, and unknown-phase for different layer definitions. From Figure 3.12 it can be seen that there are fewer (more) ice-phase (water- and unknown-phase) retrievals for single layer clouds than for two layer clouds. Figure 3.13 shows the global distribution

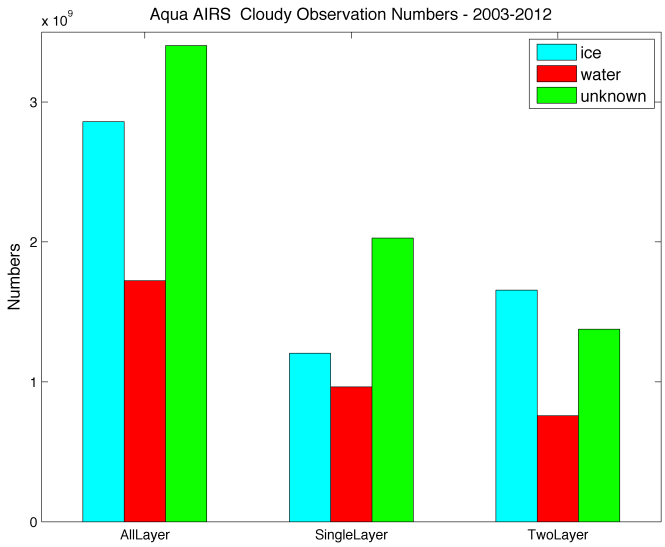

Figure 3.12: Observation numbers of filtered and gridded Aqua AIRS v6 L2 cloud thermodynamic phase for different layer cases from 2003 to 2012.

differences between two layer and single layer cases for Aqua AIRS cloud thermodynamic phase. This figure is another indication of that two layer clouds, in general, lead to more ice-phase retrievals and fewer water- and unknown-phase retrievals. The strong sensitivities to the upper cloud layer of AIRS in the multilayered cloud systems (Jin and Nasiri, 2014) may explain why ice-phase retrievals increase and water-phase retrievals decrease for two-layer cloud scenes. In addition, Figure 3.13 shows that the effect of layering is more obvious at high latitudes than in the tropics, which may be because higher thermal contrast between the cloud and the surface in the tropics making phase classification easier (Jin and Nasiri, 2014).

The effect of cloud layering on τ is given in Figure 3.14 which shows zonally averaged τ values and cumulative distribution of τ for different layer definitions. Figure 3.14 shows that while retrieved values of τ are not strongly affected by different layer definitions in most regions, single layer regimes lead to greater values of τ, especially between 40° N(S) and 50° N(S).

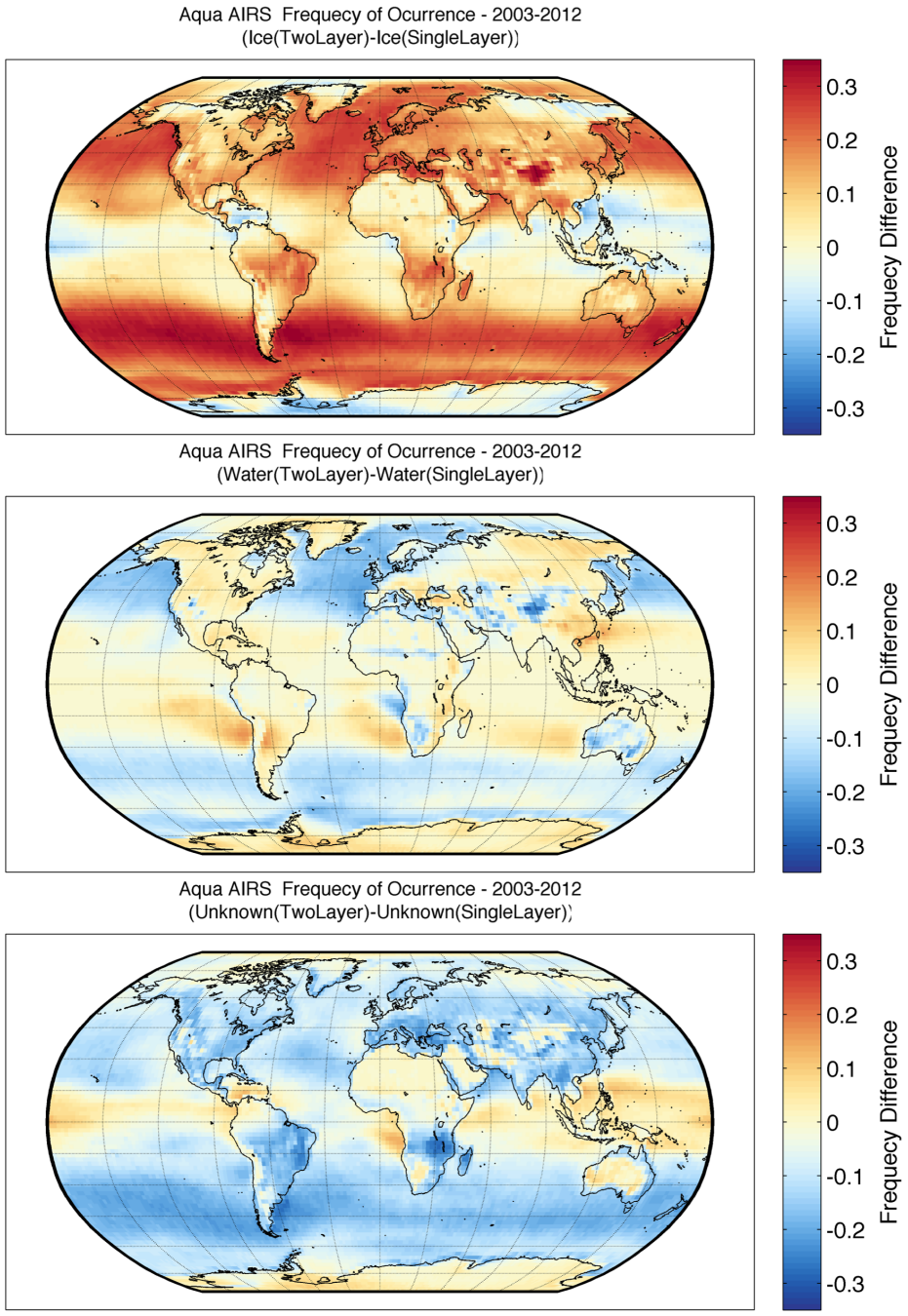

Figure 3.13: Global distribution differences of filtered and gridded Aqua AIRS v6 L2 ice-phase (top), water-phase (middle), and unknown-phase (bottom) between two layer and single layer cases for 2003 to 2012.

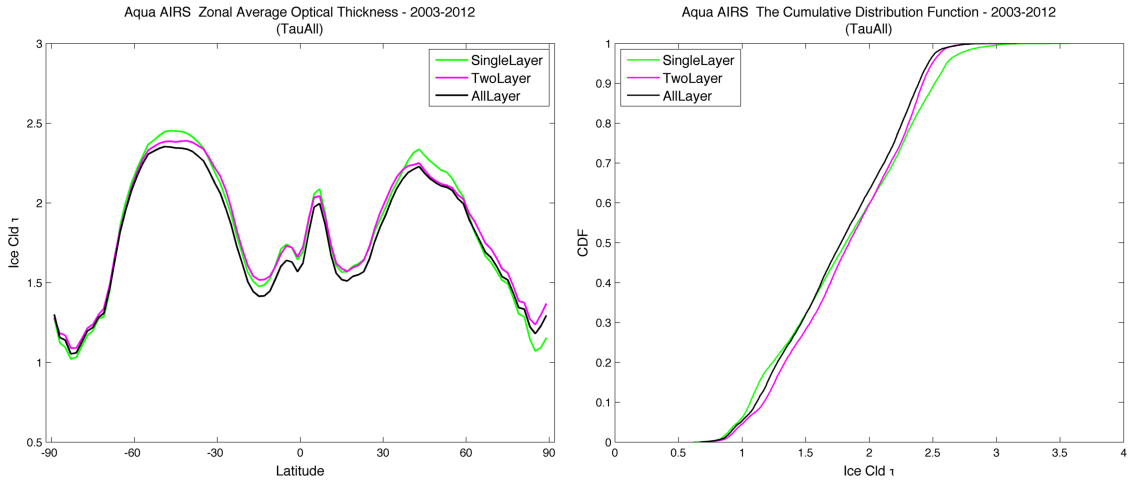

Figure 3.14: Zonally averaged values (right) and cumulative distribution (left) of filtered and gridded Aqua AIRS ice cloud optical thickness with respect to different cloud layer definitions for 2003 to 2012.

Figure 3.15 gives the zonally averaged values and cumulative distributions of low, medium, and high τ values which are summarized in Table 2.1. While the effect of layering is not strong for low and medium τ values, two layer cases lead to slightly greater values of τ. On the other hand, single layer cases yield greater τ values for high values of τ, especially in ice cloud regimes over tropics.

Figure 3.16 shows the zonally averaged D_e values and the cumulative distribution function of D_e for different layer definitions. This figure indicates that single layer cases, in general, yield smaller values of D_e. The effect of layering on effective diameter is most obvious in the tropics.

Figure 3.17 provides the same plots as Figure 3.16 for different D_e bins summarized in Table 2.1. Similar to layering the effect on τ, the effect of layering is most significant for high values of D_e.

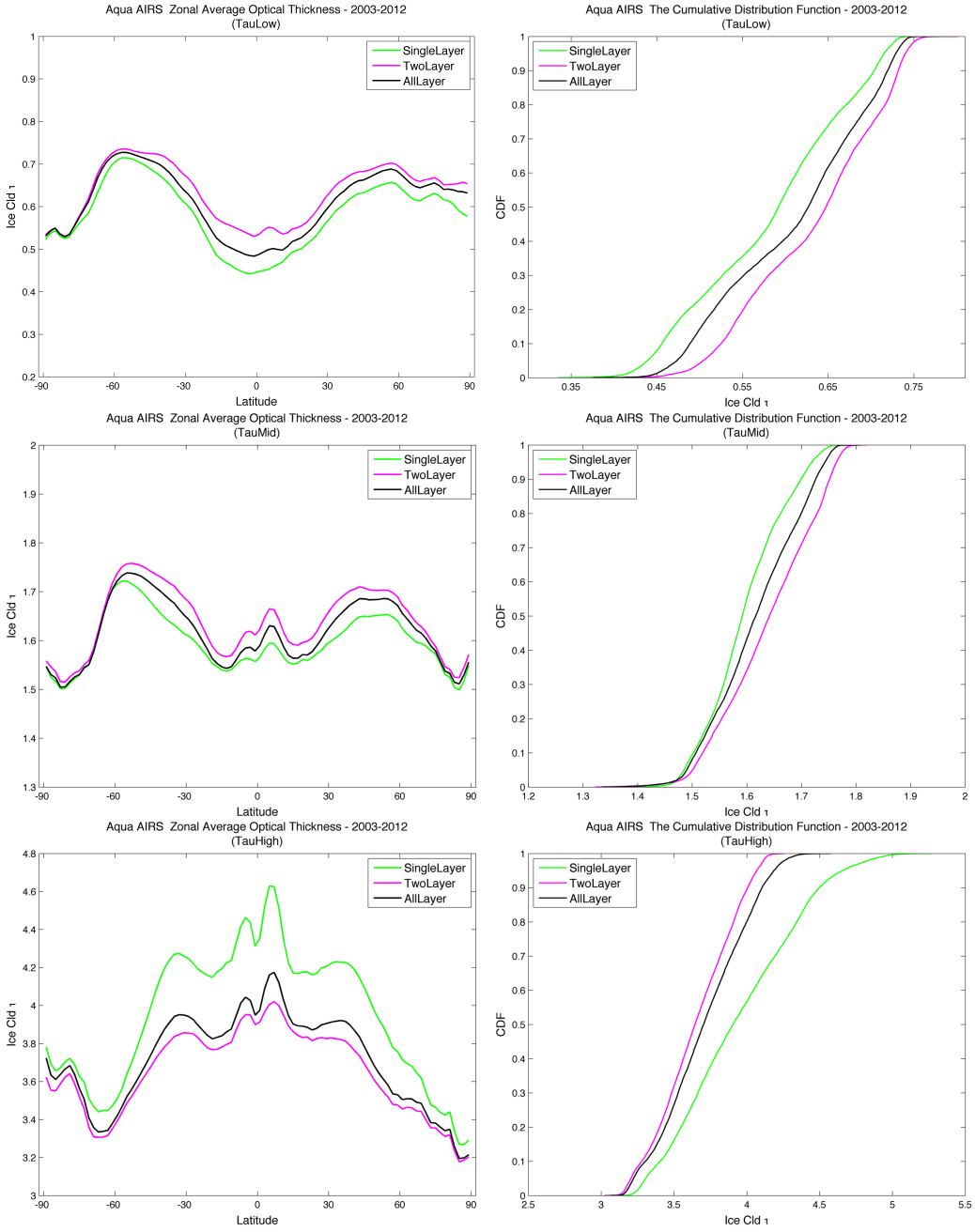

Figure 3.15: Zonally averaged values (left column) and cumulative distributions (right column) of filtered and gridded Aqua AIRS ice cloud optical thickness for low (top row), medium (middle row), and high (bottom row) values for 2003 to 2012.

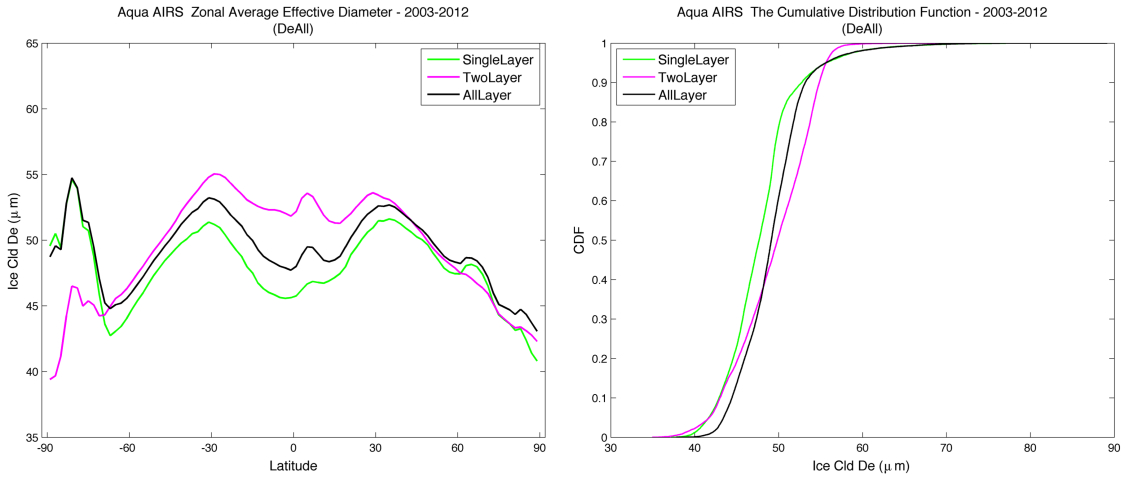

Figure 3.16: Zonally averaged values (right) and cumulative distribution (left) of filtered and gridded Aqua AIRS ice cloud effective diameter with respect to different cloud layer definitions for 2003 to 2012.

3.4 Upper Layer Cloud Top Temperature Effect

To investigate the effect of the retrieved upper layer cloud top temperature, three different temperature regimes are defined for Aqua AIRS standard Level 2 upper layer cloud top temperature (ctt). The ranges of interest are summarized in Table 2.2 (cttLow: ctt $<$ 243 K; cttMid: 243 $\leq$ ctt $<$ 273 K; cttHigh: ctt $\geq$ 273 K). Figure 3.18 shows the zonally averages of the three ctt regimes with respect to vzen cases (straight line indicates vzenLow, stars indicate vzenMid, and plus signs indicate vzenHigh). This figure indicates that satellite viewing zenith angle does not have a strong effect on the zonally averaged ctt retrieval.

Figure 3.19 shows the global average upper layer cloud top temperature difference between vzenLow and vzenHigh cases. This figure tells that higher viewing zenith angles correlate with smaller values of ctt retrievals, corresponding to warmer clouds. This is because as the viewing angle increases, the path-length between the sensor and the Earth's surface increases, which decreases the contribution by surface radiation

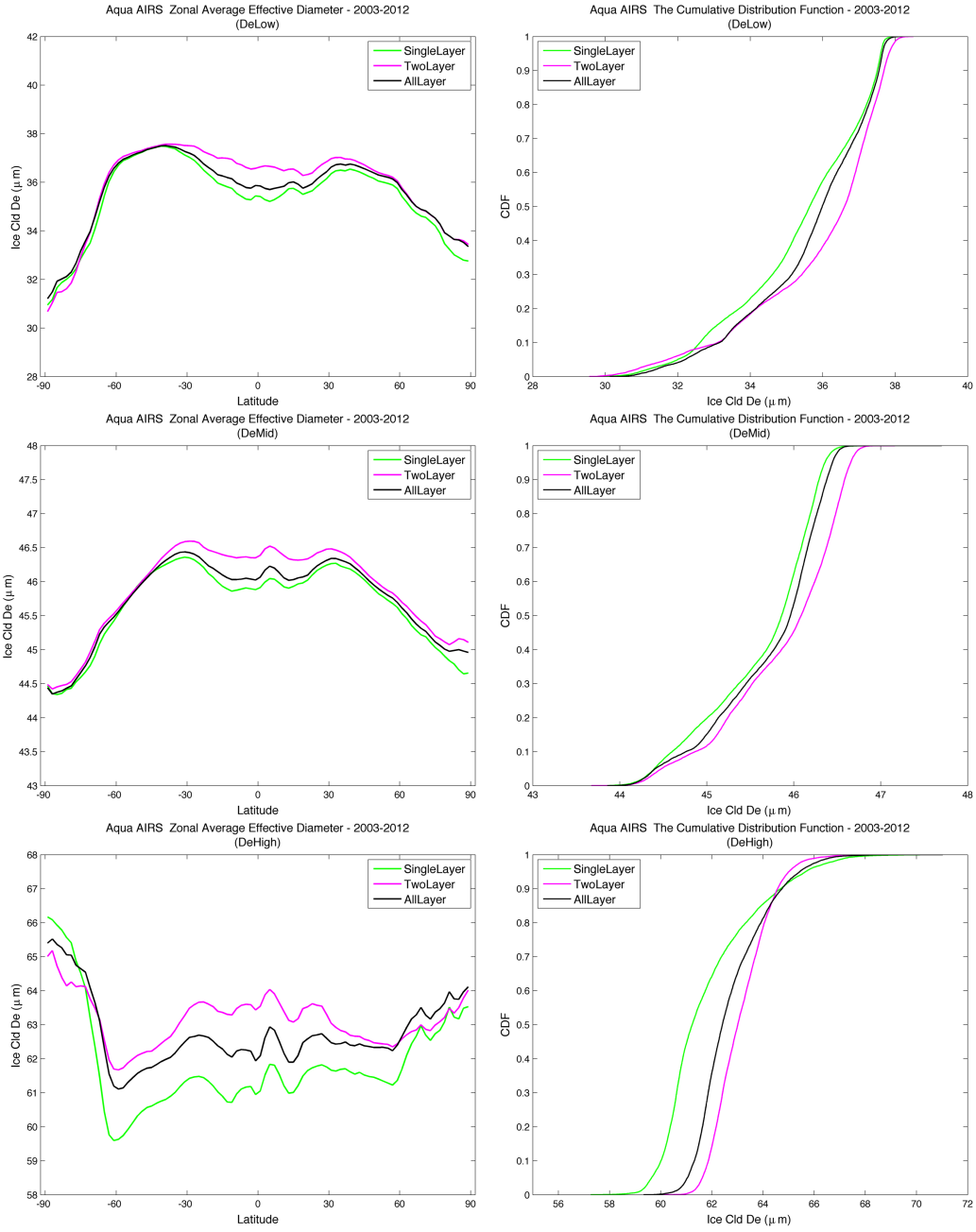

Figure 3.17: Zonally averaged values (left column) and cumulative distributions (right column) of filtered and gridded Aqua AIRS ice cloud effective diameter for low (top row), medium (middle row), and high (bottom row) values for 2003 to 2012.

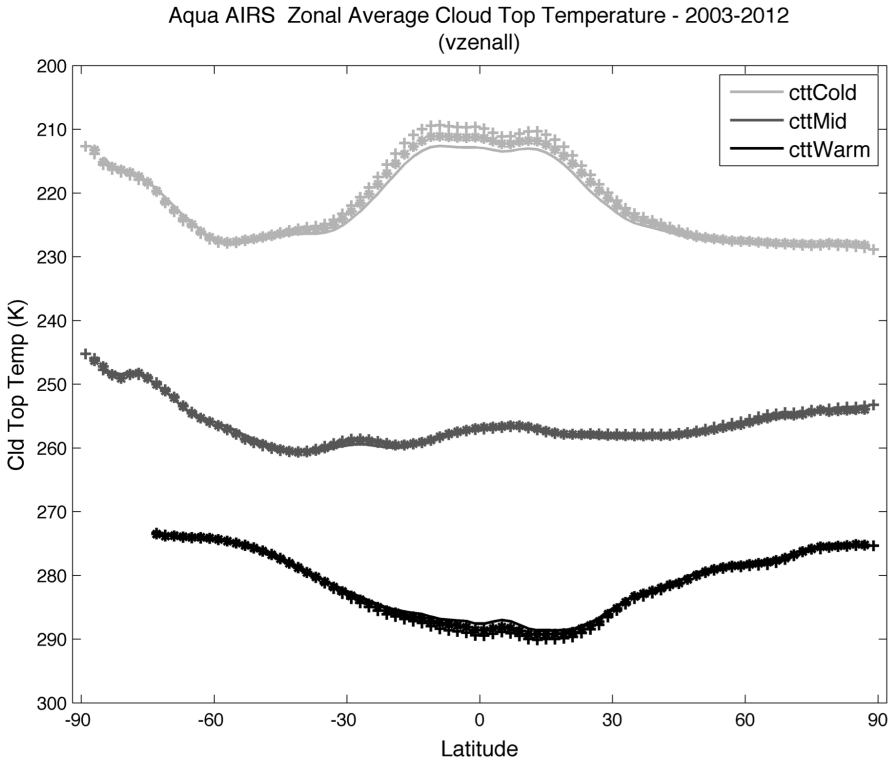

Figure 3.18: Zonally averaged values of filtered and gridded Aqua AIRS upper layer cloud top temperature with respect to different viewing zenith angles for 2003 to 2012. Straight line indicates vzenLow, stars indicate vzenMid, and plus signs indicate vzenHigh.

and increase atmospheric attenuation, thereby it becomes more likely for a cloud to be seen at a high altitude (Maddux et al., 2010). Therefore, in general, upper cloud top temperature values decrease with increasing satellite viewing angle.

The numbers of cloudy observations of Aqua AIRS ice-, water-, and unknown-phase for different ctt regimes are given in Figure 3.20. This figure shows that the number of ice clouds is the highest for cttCold regime and decreases as the temperature increases. The number of water clouds is greatest for the cttMid regime, and least for the cttCold regime. For the cttWarm and cttMid regimes, the number of the unknown phase is the highest among other phases.

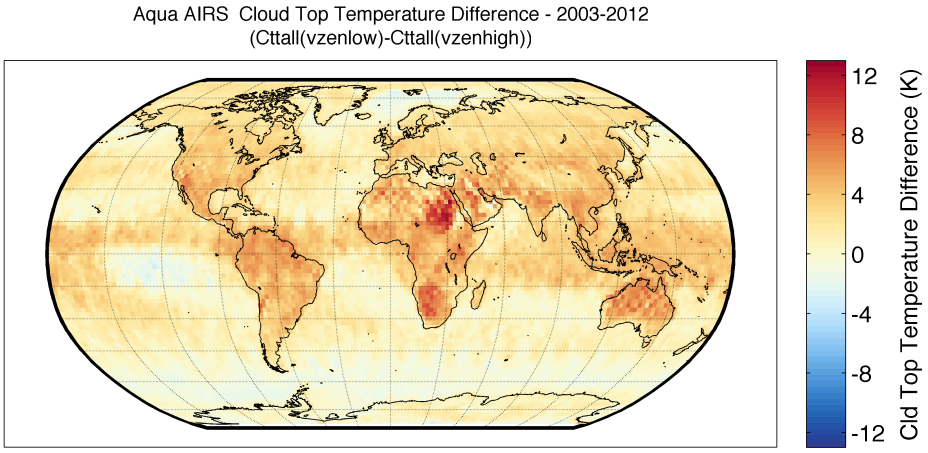

Figure 3.19: Global distribution difference of filtered and gridded Aqua AIRS v6 L2 upper layer cloud top temperature between vzenLow and vzenHigh cases for 2003 to 2012. Cttall indicates no filtering applied to the retrieval.

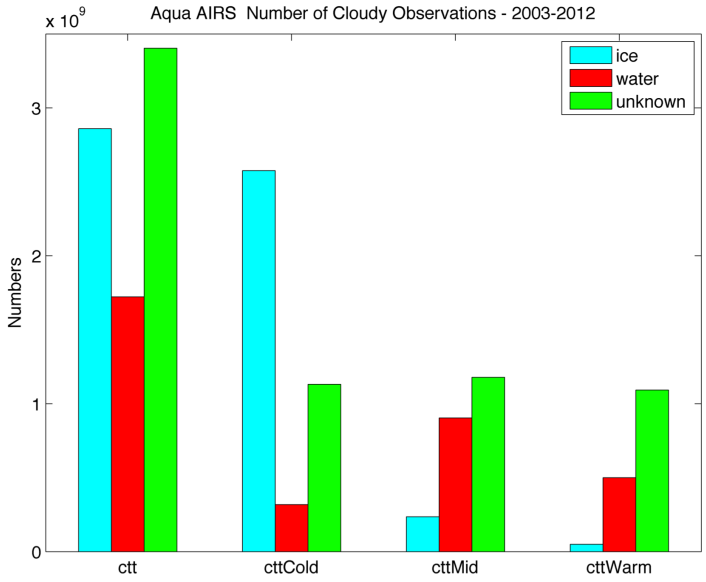

Figure 3.20: Observation numbers of filtered and gridded Aqua AIRS v6 L2 cloud thermodynamic phase for different upper layer cloud top temperature regimes from 2003 to 2012.

Figure 3.21 gives the cumulative distribution functions of ctt for ice-, water-, and unknown-phase. The figure shows that ∼90% of the ice phase cases are in the 210

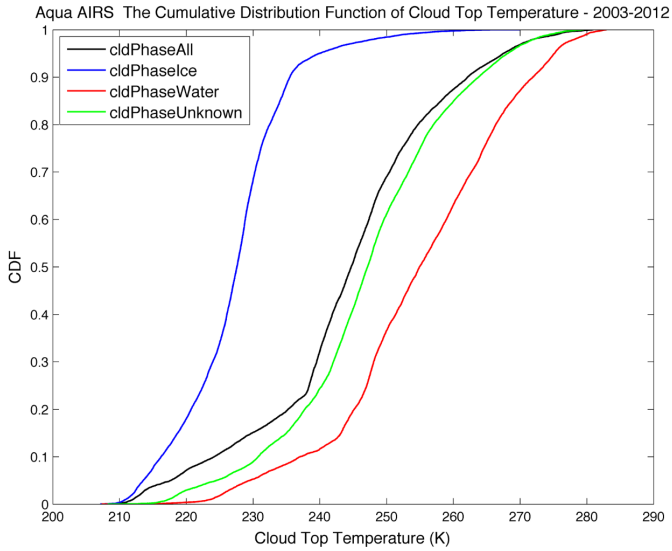

Figure 3.21: Cumulative distribution of filtered and gridded Aqua AIRS upper layer cloud top temperature with respect to cloud thermodynamic phase for 2003 to 2012.

$<$ ctt $<$ 235 K regime, which again shows the strong, and reasonable, relationship between ice phase and cttCold. Approximately 80% of the unknown cases are found at ctt between 230 and 264 K, and $\sim$80% of water cases are found between 243 and 273 K. These observations are consistent with Figure 3.20. For example, Figure 3.21 tells us that $\sim$80% of the water cases corresponds to the interval 243 $<$ ctt $<$ 273 K, which is defined as cttMid, and Figure 3.20 tells us that among the three temperature the number of water cloudy cases is highest at cttMid. Ice clouds do not occur temperatures above 270 K and only $\sim$0.05% of water clouds occur temperatures below 233 K (Figure 3.21), which shows physically reasonable agreement between two independent retrieval products (Jin and Nasiri, 2014).

4. CONCLUSIONS

In this study, the sensitives of AIRS version 6 Level 2 cloud thermodynamic phase, ice cloud optical thickness, and ice cloud effective diameter retrievals to a set of parameters are investigated for a 10 year period from 2003 to 2012. The Space-Time Gridding algorithm is used to evaluate the effects of satellite viewing zenith angle, effective cloud fraction, upper layer cloud top temperature, and cloud layering. Global cloud coverage distributions are also shown for the 10 year period, along with individual ice-, water-, and unknown-phase distributions.

The evaluation with respect to satellite viewing zenith angle shows that viewing zenith angle has minimal effects on ice-phase detection. On the other hand, higher viewing zenith angles do yield more liquid water-phase and less unknown-phase. This may be because as satellite viewing zenith angle increases, heterogeneity with the satellite's field of view increases. Kahn et al. (2011) hypothesized that this may decrease the ability of the cloud thermodynamic phase determination algorithm to classify cloud phase. Viewing zenith angle has the greatest effect on phase determination in the mid-latitudes. Also, the viewing zenith angle dependence of phase detection is not strongly affected by the time of the year, globally. The AIRS Version 6 Cloud Product includes retrievals of cloud optical thickness and effective diameter only for scenes classified as ice by the thermodynamic phase algorithm. Ice cloud optical thickness and ice cloud effective diameter retrievals show a weak dependence on viewing zenith angle. Ice cloud optical thickness tends to be greater as satellite viewing zenith angle increases.

Another implication of this study is that higher effective cloud fraction makes ice-phase and liquid water-phase detections easier; therefore, the unknown-phase

frequency decreases as the effective cloud fraction increases. This is likely because given the same cloud emissivity, the spectral phase signature is greater for higher spatial cloud fraction. Also, higher effective cloud fraction values are correlated with more ice tests passed which means greater ice-phase confidence. This is partly because one of the phase tests which relies on the brightness temperature (BT) at 960 cm^{-1}, BT at 960 cm^{-1} < 235 K, is only true for high effective cloud fraction and optical thickness. This is because cloud temperature is essentially equivalent to cloud brightness temperature for optically thick clouds. Also, for low and medium ice cloud optical thickness and ice cloud effective diameter values, higher effective cloud fractions correlate with higher values of ice cloud optical thickness and ice cloud effective diameter retrievals.

Cloud layering is shown to have a weaker effect on phase determination in the tropics than in higher latitudes. At high latitudes, ice-phase frequency is greater when there are more than one cloud layers over oceans where liquid water-phase and unknown-phase frequencies are greater when there is only one cloud layer. This may be because the strong phase sensitivity of AIRS-phase to the uppermost layer in multilayered cloud systems (Jin and Nasiri, 2014). Since scenes with two cloud layers most likely consist of a low water cloud residing underneath cirrus and the AIRS-phase is sensitive to the uppermost layer, ice-phase frequency is greater for two-layer cases than single-layer cases. Layering does not have a strong effect on ice cloud optical thickness and ice cloud effective diameter retrievals. The effect of layering on these retrievals is the most obvious for high values of ice cloud optical thickness and effective diameter retrievals.

This study also shows that low, medium, and high upper level cloud top temperature retrievals are not strongly affected by viewing zenith angle. However, since higher viewing zenith angles increase the probability to see a cloud higher in the

atmosphere (Maddux et al., 2010), the global average of upper cloud top temperature is generally greater, corresponding to warmer clouds, for lower viewing angles. According to this study, approximately 90% of the ice phase retrievals are found at upper level cloud top temperature between 210 and 235 K which shows that most of the clouds with upper cloud top temperatures lower than 235 K are composed of ice. ∼80% of the unknown phase cases have upper level cloud top temperature values between 230 and 264 K, and approximately 80% of the water phase retrievals are between 243 and 273 K upper level cloud top temperature values.

These results show that users of Aqua AIRS version 6 Level 2 cloud phase retrieval should consider the satellite viewing zenith angle effect on AIRS-phase especially for liquid water and unknown phases. Another point to consider when using the cloud products is effective cloud fraction because higher values of it makes phase detection easier. In addition, the sensitivity of AIRS-phase to the uppermost layer when there are more than one cloud layer is another important point that users should take into account. In general, these effects, especially viewing zenith angle and layering effects, are weaker in tropics than in high latitudes, which may be because higher thermal contrast between the cloud and the surface in the tropics makes phase classification easier over tropics (Jin and Nasiri, 2014). Therefore, usage of the products requires more attention for the high latitudes. While these effects are not strong for ice cloud optical thickness and ice cloud effective diameter retrievals, the effects are needed to be considered for carefully analysis of the retrievals. Indeed, ice cloud optical thickness and ice cloud effective diameter dependences may require more investigations.

These results, therefore, suggest that a viewing zenith angle correction should be developed and implemented for the next version of AIRS cloud products algorithm. By considering the above mentioned effects on Aqua AIRS cloud thermodynamic

phase, ice cloud optical thickness, and ice cloud effective diameter, one can decrease the effects of non-physical artifacts, so that the accuracy of interpreting the AIRS data could be enhanced. Thus, reliability of the products would be better for comparing with either other instruments' cloud products or model-derived cloud products.

REFERENCES

Aumann, H. H., et al., 2003: AIRS/AMSU/HSB on the Aqua mission: Design, science objectives, data products, and processing systems. *Geoscience and Remote Sensing, IEEE Transactions on*, **41 (2)**, 253–264, doi:10.1109/TGRS.2002.808356.

Bony, S., M. Webb, C. Bretherton, S. Klein, P. Siebesma, G. Tselioudis, and M. Zhang, 2011: CFMIP: Towards a better evaluation and understanding of clouds and cloud feedbacks in CMIP5 models. *CLIVAR Exchanges*, **16 (2)**, 20–23.

Boucher, O., et al., 2013: Clouds and aerosols. *Climate Change 2013: The Physical Science Basis. Contribution of Working Group I to the Fifth Assessment Report of the Intergovernmental Panel on Climate Change*, T. F. Stocker, D. Qin, G.-K. Plattner, M. Tignor, S. K. Allen, J. Boschung, A. Nauels, Y. Xia, V. Bex, and P. M. Midgley, Eds., Cambridge University Press, Cambridge, United Kingdom and New York, NY, USA, 571–657.

Bowman, K., et al., 2006: Tropospheric emission spectrometer: Retrieval method and error analysis. *Geoscience and Remote Sensing, IEEE Transactions on*, **44 (5)**, 1297–1307, doi:10.1109/TGRS.2006.871234.

Campbell, G. G., 2004: View angle dependence of cloudiness and the trend in ISCCP cloudiness. *13th Conference on Satellite Meteorology and Oceanography*, Norfolk, Va., Amer. Meteor. Soc., P6.7, [Available online at `http://ams.confex.com/ams/pdfpapers/79041.pdf`].

Evan, A. T., A. K. Heidinger, and D. J. Vimont, 2007: Arguments against a physical

long-term trend in global ISCCP cloud amounts. *Geophysical Research Letters*, **34 (4)**, L04 701, doi:10.1029/2006GL028083.

Jiang, J. H., et al., 2012: Evaluation of cloud and water vapor simulations in CMIP5 climate models using NASA "A-Train" satellite observations. *Journal of Geophysical Research: Atmospheres*, **117 (D14)**, D14 105, doi:10.1029/2011JD017237.

Jin, H., 2012: Satellite remote sensing of mid-level clouds. Ph.D. thesis, Texas A&M University, 159 pp.

Jin, H. and S. L. Nasiri, 2014: Evaluation of AIRS cloud thermodynamic phase determination with CALIPSO. *Journal of Applied Meteorology and Climatology*, doi:10.1175/JAMC-D-13-0137.1.

Joyce, R., J. Janowiak, and G. Huffman, 2001: Latitudinally and seasonally dependent zenith-angle corrections for geostationary satellite IR brightness temperatures. *Journal of Applied Meteorology*, **40 (4)**, 689–703, doi:10.1175/1520-0450(2001)040¡0689:LASDZA¿2.0.CO;2.

Kahn, B. H., S. L. Nasiri, M. M. Schreier, and B. A. Baum, 2011: Impacts of subpixel cloud heterogeneity on infrared thermodynamic phase assessment. *Journal of Geophysical Research: Atmospheres*, **116 (D20)**, D20 201, doi:10.1029/2011JD015774.

Kahn, B. H., et al., 2003: Near micron-sized cirrus cloud particles in high-resolution infrared spectra: An orographic case study. *Geophysical Research Letters*, **30 (8)**, 1441, doi:10.1029/2003GL016909.

Kahn, B. H., et al., 2008: Cloud type comparisons of AIRS, CloudSat, and CALIPSO cloud height and amount. *Atmospheric Chemistry and Physics*, **8 (5)**, 1231–1248, doi:10.5194/acp-8-1231-2008.

Kahn, B. H., et al., 2014: The atmospheric infrared sounder version 6 cloud products. *Atmospheric Chemistry and Physics*, **14 (1)**, 399–426, doi:10.5194/acp-14-399-2014.

Kinne, S. and K. N. Liou, 1989: The effects of the nonsphericity and size distributions of ice crystals on the radiative properties of cirrus clouds. *Atmospheric Research*, **24**, 273–284, doi:10.1016/0169-8095(89)90049-5.

Lin, B., P. Minnis, T. F. Fan, Y. Hu, and W. Sun, 2010: Radiation characteristics of low and high clouds in different oceanic regions observed by CERES and MODIS. *International Journal of Remote Sensing*, **31 (24)**, 6473–6492, doi:10.1080/01431160903548005.

Loeb, N. G., B. A. Wielicki, D. R. Doelling, G. L. Smith, D. F. Keyes, S. Kato, N. Manalo-Smith, and T. Wong, 2009: Toward optimal closure of the earth's top-of-atmosphere radiation budget. *Journal of Climate*, **22 (3)**, 748–766, doi:10.1175/2008JCLI2637.1.

Maddux, B. C., S. A. Ackerman, and S. Platnick, 2010: Viewing geometry dependencies in MODIS cloud products. *Journal of Atmospheric and Oceanic Technology*, **27 (9)**, 1519–1528, doi:10.1175/2010JTECHA1432.1.

Minnis, P., D. P. Garber, D. F. Young, R. F. Arduini, and Y. Takano, 1998: Parameterizations of reflectance and effective emittance for satellite remote sensing of cloud properties. *Journal of the Atmospheric Sciences*, **55 (22)**, 3313–3339, doi:10.1175/1520-0469(1998)055<3313:PORAEE>2.0.CO;2.

Minnis, P., K.-N. Liou, and Y. Takano, 1993: Inference of cirrus cloud properties using satellite-observed visible and infrared radiances. Part I: Parameterization

of radiance fields. *Journal of the Atmospheric Sciences*, **50 (9)**, 1279–1304, doi:10.1175/1520-0469(1993)050<1279:IOCCPU>2.0.CO;2.

Nam, C., S. Bony, J.-L. Dufresne, and H. Chepfer, 2012: The 'too few, too bright' tropical low-cloud problem in CMIP5 models. *Geophysical Research Letters*, **39 (21)**, L218 201, doi:10.1029/2012GL053421.

Nasiri, S. L. and B. H. Kahn, 2008: Limitations of bispectral infrared cloud phase determination and potential for improvement. *Journal of Applied Meteorology and Climatology*, **47 (11)**, 2895–2910, doi:10.1175/2008JAMC1879.1.

Norris, J. R., 2011: Multidecadal changes in near-global cloud cover and estimated cloud cover radiative forcing. *Journal of Geophysical Research*, **110**, D08 206, doi:10.1029/2004JD005600.

Smith, N., W. P. Menzel, E. Weisz, A. K. Heidinger, and B. A. Baum, 2013: A uniform space-time gridding algorithm for comparison of satellite data products: Characterization and sensitivity study. *Journal of Applied Meteorology and Climatology*, **52 (1)**, 255–268, doi:10.1175/JAMC-D-12-031.1.

Stocker, T., et al., 2013: *Climate Change 2013: The Physical Science Basis. Contribution of Working Group I to the Fifth Assessment Report of the Intergovernmental Panel on Climate Change*. Cambridge University Press, Cambridge, United Kingdom and New York, NY, USA, 1535 pp.

Strabala, K. I., S. A. Ackerman, and W. P. Menzel, 1994: Cloud properties inferred from 8-12-μm data. *Journal of Applied Meteorology*, **33 (2)**, 212–229, doi:10.1175/1520-0450(1994)033<0212:CPIFD>2.0.CO;2.

Susskind, J., C. Barnet, and J. Blaisdell, 2003: Retrieval of atmospheric and surface parameters from AIRS/AMSU/HSB data in the presence of clouds. *Geoscience and Remote Sensing, IEEE Transactions on*, **41 (2)**, 390–409, doi: 10.1109/TGRS.2002.808236.

Wielicki, B. A., E. F. Harrison, R. D. Cess, M. D. King, and D. A. Randall, 1995: Mission to planet earth: Role of clouds and radiation in climate. *Bulletin of the American Meteorological Society*, **76 (11)**, 2125–2153, doi:10.1175/1520-0477(1995)076<2125:MTPERO>2.0.CO;2.

Wylie, D., D. L. Jackson, W. P. Menzel, and J. J. Bates, 2005: Trends in global cloud cover in two decades of HIRS observations. *Journal of Climate*, **18 (15)**, 3021–3031, doi:10.1175/JCLI3461.1.

Yang, Y. and L. Di Girolamo, 2008: Impacts of 3-D radiative effects on satellite cloud detection and their consequences on cloud fraction and aerosol optical depth retrievals. *Journal of Geophysical Research: Atmospheres*, **113 (D4)**, D04 213, doi:10.1029/2007JD009095.